[Mg(H2O)4][(VO)2(PO4)2]: Crystal structure, DFT calculations, and catalytic activity

Mohamed Akouibaa, Nouhaila El Amin, Ahmed Soussi, Brahim El Bali, Mohamed Lachkar, Saïd Obbade, Laurent Jouffret

$[Mg(H_2O)_4][(VO)_2(PO_4)_2]$: Crystal Structure, DFT Calculations, and Catalytic Activity

Mohamed Akouibaa [1], Nouhaila El Amin[1], Ahmed Soussi [2], Brahim El Bali [3], Mohamed Lachkar [1], Saïd Obbade [4] and Laurent Jouffret [5]

[1]*Engineering Laboratory of Organometallic, Molecular Materials and Environment, Faculty of Sciences, Sidi Mohammed Ben Abdellah University, 30000 Fez, Morocco.*
[2] Materials and Renewable Energy Laboratory, Ibn Zohr University, BP8106, Agadir, Morocco.

[3] Independent Scientist, Marrakech, Morocco; ORCID: 0000-0001-6926-6286, Email: b_elbali@yahoo.com

[4] Laboratoire LEPMI, Université Grenoble Alpes, 38402 St Martin d'Hères Cedex, France.

[5] Institut de Chimie de Clermont-Ferrand - UMR 6296, Université Clermont Auvergne, 24, Avenue Blaise Pascal, 63178 Aubière Cedex, France.

Abstract

$[Mg(H_2O)_4][(VO)_2(PO_4)_2]$ has been successfully synthesized in the M^{2+}-V^{4+}-P-O system through hydrothermal synthesis route. It was characterized using single-crystal X-ray diffraction, Fourier Transform Infrared Spectroscopy (FT-IR), scanning electron microscopy (SEM), and thermal stability analysis (TG-DTA). $[Mg(H_2O)_4][(VO)_2(PO_4)_2]$ crystallizes in the tetragonal system (S.G.: I4/m), with the cell parameters: a= 6.2497(3), b= 6.2497(3), c= 13.4194(8) Å, V= 524.145Å^3, and Z= 2. The structure consists of vanadyl phosphate layers $[VO(PO_4)]_{2\infty}$, constructed from O-vertices sharing $[VO_5]$-square pyramids and $[PO_4]$ tetrahedral, which are separated by layers of $[MgO_6]$ octahedral linked to $[VO_5]$ by Mg-O-V bonds along *c*-axis. FT-IR confirmed the characteristic bands of phosphate and the vanadium (IV) groups. Moreover, thermogravimetric analysis of the complex has been used to investigate its thermal behavior. Furthermore, the catalytic efficiency of the title compound in the reduction by $NaBH_4$ of three nitrophenol isomers (ortho-, meta-, and para-) to their corresponding aminophenols was tested. All three nitrophenol isomers could be reduced in 30 sec in the presence of the title compound. First-principles calculations employing density functional theory (DFT) explored the structural, electronic, and optical properties. These computations were utilized to analyze the band structure, density of states, reflectivity, absorption coefficient, refractive index, and extinction coefficient. Examining the band structure and density of states (DOS) reveals that the material possesses a band gap of 2.79 eV.

Keywords: Vanadium, Phosphate, Crystal structure, catalysis, DFT calculations.

Introduction

Vanado-phosphates have been selected in the course of evolution since their prospective primarily utilization as complex catalytic systems. They have been extensively studied as catalysts for the oxidation of light hydrocarbons to maleic anhydride or as precursors of catalysts for selective oxidations. As electrode materials, they have been tested in lithium-ion batteries as in: $Li_5VO(PO_4)_2$ [1], $Li_4VO(PO_4)_2$ [2] and $Li_2(VO)_2(HPO_4)_2(C_2O_4)\cdot 6H_2O$ [3]; in sodium-ion batteries $NaVOPO_4$ [4], $Na_3(VO)_2(PO_4)_2F$ [5] and $Na_3(VO)_2(PO_4)_2F$@C [6]; and potassium-ion batteries β-$K(VO_2)_2(PO_4)$ [7] and $K_6(VO)_2(V_2O_3)_2(PO_4)_4(P_2O_7)$ [8]. Moreover, they have been tested as pseudo capacitors like in $VOPO_4$-graphene [9] or sensors for polyaniline/vanadyl phosphate (PANI-$VOPO_4$) and $Na_{0.5}VOPO_4\cdot 2H_2O$ [10, 11]. They have been applied in the environment as anti-corrosion coatings, such as in the P-M/epoxy composites $M_{0.5}VOPO_4$ (where M= Mg, Ni, and Zn) [12]. In vanado-phosphates, V can exhibit various coordinations (4-6) and variable oxidation states (III, IV, V). Consequently, different various environments to host Li-ion [13]. Because of the low cost and the high oxidation potential of the V^{3+}/V^{4+} redox couple (-4 V), vanado-phosphates might be an alternative to the existing commercial $LiCoO_2$-based cathode materials [14, 15]. The ability of V as a cation (V^{3+}, VO^{2+}, VO_2^{+}) to behave much the same as a typical transition metal has attracted systematic attention. As a result, many new MVOPOs have been prepared over the last ten years using different synthetic routes. Anhydrous vanado-phosphates have been studied from alkali alkaline earth metals and transition metals. For instance, within this family, there are compounds of the gross formula $A(VO)(PO_4)_2$ like that were first discovered $Zn_2VO(PO_4)_2$ [16], followed by $Mn_2VO(PO_4)_2.H_2O$ [17], then has been prepared $Sr_2(VO)(PO_4)_2$ [18], and $Pb_2VO(PO_4)$ [19, 20]. our attention was drawn toward the experimental realizations that are very scarce and currently restricted to two families of layered vanadium phosphates and oxide compounds. Various and recent studies have

investigated the magnetic proprieties of $AA'VO(PO_4)_2$ (AA′ = BaZn, SrZn, BaCd, and PbZn) [21-24], and Li_2VOXO_4 (X= Si, Ge) [25-29]. Furthermore, the layered mixed-valence vanado-phosphates hydrates $A(VO)_2(PO4)_2.xH_2O$ remain mostly unexplored among these structures. Up to now, it has been only reported $A(VO)_2(PO_4)_2.4H_2O$ with (A= Sr, Co, Ni, Pb, Ca, Ba, Cd, Ag) in the literature was described some time ago [30], and by hydrothermal synthesis, were a new vanadyl (IV) compound has been synthesized $Rb_2Cu(VO_2)_2(PO_4)_2$ [31], NaVPO4F [32] and $Na_3(VO)_2(PO_4)_2F$ [33].

This work aimed to synthesize new compounds of stoichiometry $A(VO)_2(PO_4)_2.nH_2O$, where A is an alkaline earth metal. The impetus that encouraged us to do this research was the expectation of discovering new structure types that have interesting electrochemical performance and valuable physical properties, which would be owned. In this article, we report herein mild hydrothermal synthesis, crystal structure, FT-IR spectroscopy, and thermal behavior of a new Magnesium(II) Vanadyl(IV) phosphate compound: $[Mg(H_2O)_4][(VO)_2(PO_4)_2]$. This method was adopted because it was considered the most beneficial method according to the previous studies, and the result was proven based on X-ray analysis and infrared spectroscopy. This study also looks at theoretical findings about the structure, electronic, and optical of $[Mg(H_2O)_4][(VO)_2(PO_4)_2]$. We used first-principles calculations within the DFT framework, specifically the PBE-GGA approximation, with the WIEN2K software package. This method helps analyze the properties of $[Mg(H_2O)_4][(VO)_2(PO_4)_2]$ and produces results similar to those from the hydrothermal method.

2. Experimental

2.1. Materials and instrumentation

All chemicals (reagents and solvents) used for the synthesis were used as received. Purity and supplier should be reported for each starting reagent. The crystalline product was

characterized by single-crystal X-ray diffraction analysis, Fourier Transform Infrared spectroscopy (FTIR), scanning electron microscopy (SEM), and Thermal Gravimetric analysis (TG-DSC). The single-crystal X-ray diffraction observations were performed at 173 K utilizing Mo-Kα radiation (λ = 0.71093 Å) and a Bruker APEX-II CCD diffractometer. With a VERTEX 70 FTIR instrument (400–4000 cm^{-1}), the FTIR spectra were recorded using the ATR method with a resolution of 4 cm^{-1} at room temperature. TG analysis was carried out using a Diamond TGA/DTA equipment (Perkin-Elmer) thermal analyzer (25-1000 °C) in the air at a 10 °C/min heating rate. The catalytic activity of $[Mg(H_2O)_4][(VO)_2(PO_4)_2]$, in the reduction of the three nitrophenol isomers (2-NP, 3-NP, and 4-NP) to their corresponding aminophenols, was assessed using a Camspec M550 double beam scanning UV-Visible spectrophotometer.

2.2. Synthesis of $[Mg(H_2O)_4][(VO)_2(PO_4)_2]$

Reagent-grade chemicals were used as received from Sigma-Aldrich and employed without additional purification. The novel bimetallic phosphate $[Mg(H_2O)_4][(VO)_2(PO_4)_2]$ was prepared using a single step by employing mild hydrothermal methods. Stoichiometric mixtures of V_2O_5, MgO, and H_3PO_4 were used in the synthesis. First, an adequate mixture of V_2O_5 and MgO was dissolved in distilled water (10 mL) to form a cloudy solution (Solution A), then H_3PO_4 was added dropwise under constant stirring, and the resulting mixture, with a pH value of about 1.5, was sealed in a Teflon-lined steel autoclave and heated at 200 °C for 2 days. After cooling to room temperature, green Plate-like crystals were obtained by filtration, washed with distilled water, and dried in air.

2.3. X-ray powder diffraction

The phase purity of the title compound was confirmed by Powder diffraction performed on a Rigaku Smartlab equipped with a high-temperature chamber Anton-Paar HTK 1200N in Bragg-Brentano geometry using Cu Kα radiation, λ= 1.54051 Å, and detector Hypix-3000 in

2D mode scan. The 2θ scan range was 5-80° with a step size on 2θ of 0.01°. The XRD pattern was consistent with the structure determined using the single-crystal XRD. A least square fit of the powder XRD lines (CuKα) using the (hkl) indices generated from single-crystal X-ray data gave the cell parameters, which are in good agreement with those determined by single-crystal XRD (Fig. 1). Furthermore, their diffraction peaks are consistent with the simulated, indicating the purity of the as-synthesized products. The differences in intensities between the experimental and simulated XRPD patterns may be due to the variation in the preferred orientation of the powder sample during the collection of the experimental XRPD pattern [34].

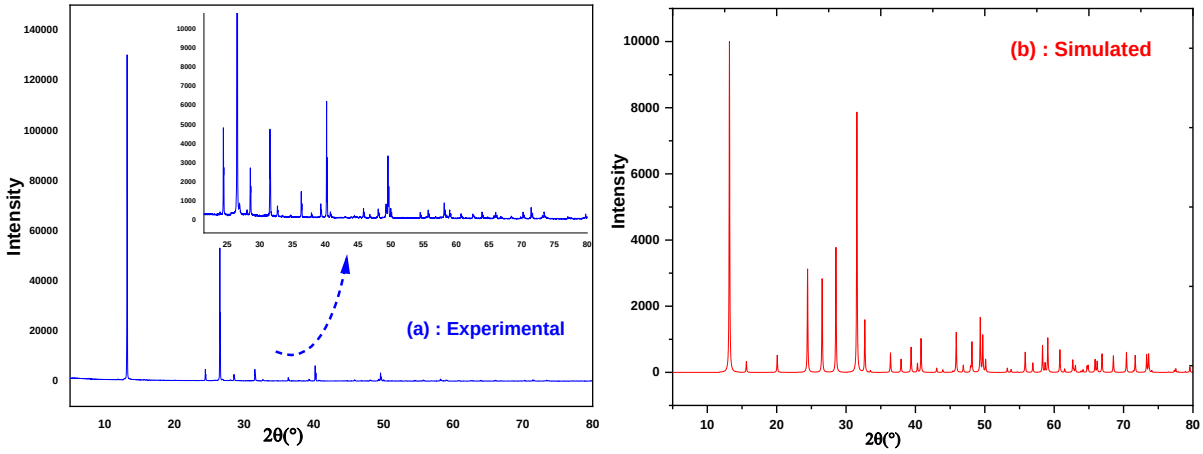

Fig. 1: Powder X-ray diffraction pattern for $(H_2en)[Mg(H_2O)_2(C_2O_4)_2]$, (a) experimental and (b) simulated.

2.4. Single crystal study

For X-ray diffraction examination, a suitable crystal with the dimensions of 0.28×0.27×0.08 mm^3 was selected. The MoKα radiation (λ = 0.71073 Å) was used to collect data at 173 K using a Bruker APEX-II CCD diffractometer. The *CrysAlis* program suite was used for unit cell determination, data collection and reduction, and analytical absorption corrections [35]. The crystal structure for the molecule in the title has been determined using direct methods and serial Fourier difference syntheses and then refined using the SHELX suite's weighted full-matrix least squares method against F^2 [36]. The *I*4/*m* space group describes the

Tetragonal structure that corresponds to it. The non-hydrogen atoms were refined in anisotropic approximation. The differential density allowed for easy identification of each H atom. All calculations were carried out using the WinGX software package [37]. The DIAMOND program was used to draw the structural graphics [38]. The main crystallographic data, data collection, and structure refinement information are summarized in Table 1. Tables 2 and 3 present basic geometrical information and atomic coordinates, respectively.

Table 1. Crystal data and structure refinement parameters for $[Mg(H_2O)_4][(VO)_2(PO_4)_2]$.

Parameters	**compound**
Chemical formula	$H_8MgO_{14}P_2V_2$
M_r	420.19
Crystal system, space group	Tetragonal, *I4/m*
Temperature (K)	173
a, *b*, *c* (Å)	6.2497 (3) , 6.2497 (3) , 13.4194 (8)
V (Å^3)	524.14 (6)
Z	2
Radiation type	Mo *K*α (λ = 0.71073 Å)
μ (mm^{-1})	2.23
Crystal size (mm)	0.28 × 0.27 × 0.08
Color	Plate, green
θ Range (°)	3-34
F(000) / D_x (g.cm^{-3})	416/2.662
Index ranges	-9≤h≤9, -9≤ k ≤9, -20≤ l ≤20
Diffractometer	Bruker APEX-II CCD
Absorption correction	numerical Bruker (2001). *SADABS*. Bruker AXS Inc., Madison, Wisconsin, USA.
T_{min}, T_{max}	0.633, 0.878
No. of measured, independent and observed [$I > 2\sigma(I)$] reflections	21902, 547, 540
Refinement method	Full-matrix least-squares on $\|\mathbf{F}^2\|$
R_{int}	0.026
$R[F^2 > 2\sigma(F^2)]$, $wR(F^2)$, *S*	0.015, 0.044, 1.20

No. of reflections	547
No. of parameters	29
$\Delta\rho_{max}$, $\Delta\rho_{min}$ (e Å^{-3})	0.52, -0.32

2.5. Reduction process of nitrophenol isomers

The reduction of the three-nitrophenol isomers (4-NP, 3-NP, and 2-NP) to aminophenol isomers was used to assess the compound catalytic activity (4-AP, 3-AP, and 2-AP). Using a Camspec M550 double-beam scanning UV-visible spectrophotometer, the concentration fluctuations of the three-nitrophenol isomers during their catalytic transformation in the presence of the Magnesium(II) vanadyl(IV) phosphate $[Mg(H_2O)_4][(VO)_2(PO_4)_2]$, were monitored an experimental protocol as defined previously in the literature [39, 40]. In fact, a conventional test involved mixing (40 mL) of a 4×10^{-4} M aqueous solution of one of the three isomers of nitrophenol, such as 2-nitrophenol, 3-nitrophenol, or 4-nitrophenol, with (40 mL) of an 8×10^{-4} M aqueous solution of sodium tetrahydroborate ($NaBH_4$) while stirring continuously at room temperature. After commencing the reaction without a catalyst, the color of the solution abruptly changes to a dark yellow tint due to the creation of the nitrophenolate ion. At the same time, absorption peaks were observed at (nm) 401, 393, and 415 for para-nitrophenol, meta-nitrophenol, and ortho-nitrophenol. The $[Mg(H_2O)_4][(VO)_2(PO_4)_2]$ (0.05 g) was then added to the aqueous solution under continuous stirring, and it resulted in the disappearance of the dark yellow color of the solution under the effect of the catalyst. This reduction reaction was monitored via UV-Vis spectra measurements.

3. Results and discussion

3.1 Crystal structure´s description

The building of the asymmetric unit compound is formed by six non-hydrogen atoms consisting of one Mg atom, three O atoms (including one hydroxyl), one P, and one V as

depicted in Fig. 2. The crystal structure of $[Mg(H_2O)_4][(VO)_2(PO_4)_2]$ consists in $[VO(PO_4)]$ layers, built upon corner-sharing $[VO_5]$- square pyramids and $[PO_4]$-tetrahedra, which layers host Mg^{2+} in octahedral cavities (Fig. 3).

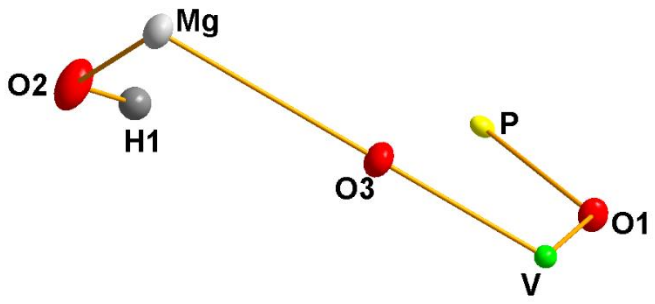

Fig. 2: Asymmetric unit in the crystal structure of $[Mg(H_2O)_4][(VO)_2(PO_4)_2]$.

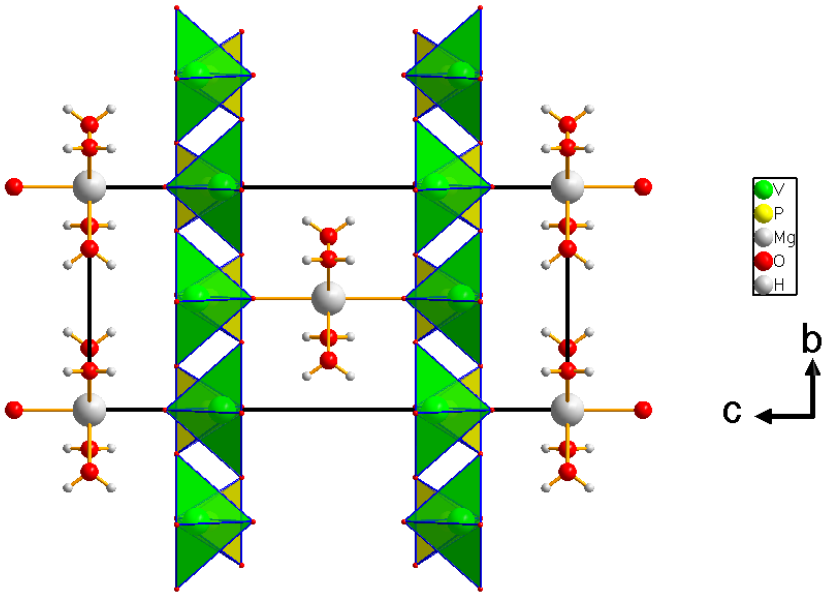

Fig. 3: A projection along a-axis of the crystal structure of $[Mg(H_2O)_4][(VO)_2(PO_4)_2]$, showing the $[(VO)(PO_4)]$ layers interconnected by $[Mg(H_2O)_4]^{2+}$ groups.

The vanadyl phosphate planes of the compound exhibit the $[(VO)_2(\mu_2\text{-}PO_4)_2]$ unit, which is a characteristic structural motif of the lamellar $[VO(PO_4)]$ class of materials (Fig. 4). When viewed along the b-axis, the square pyramids of VO5 direct the vertex occupied by the apical

oxo-vanadyl alternately up and down relative to the layer. Neighboring layers are aligned to order the oxo-groups of corresponding vanadyl sites directly toward the midpoints of these O-O vectors, with Mg-O distances of 2.1180 Å.

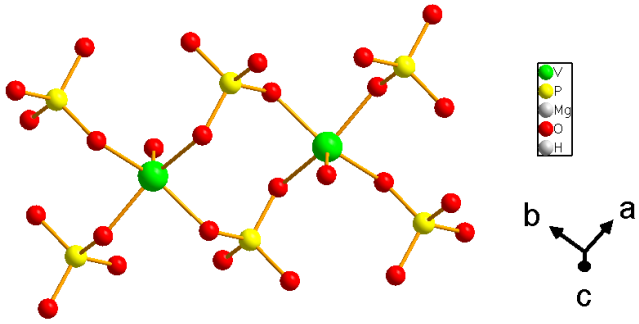

Fig. 4: The $[(VO)_2(\mu_2\text{-}PO_4)_2]$ structural motif

Valence-sum calculations (BVS) resulted in a value of 4,15 for the V site, which is very close to the ideal value of 4 for V^{4+} [40]. The divalent cation Mg^{2+} ion lies in a special position and has D4h symmetry; it is coordinated by six O atoms which four belong to water molecules lying in the equatorial plane with the Mg–O distances of 2.1180 Å and two axial O atoms, from the vanadyl(IV) oxo atoms of two adjacent layers, each has a Mg-O distance of 2.1180 Å, which adopting an octahedron rearrangement $[Mg(H_2O)_4(VO)_2]$, these distance are similar which to the mean distances in $Rb[Mg(H_2O)_6](PO_4)$ [29] and $[Co(H_2O)_4][(VO)_2(PO_4)_2]$ [42], and a slightly lower (av. 1.974 Å) than the value reported in $Mg_{1-x}Zn_x(VOPO4)2{\cdot}4H2O$ (x ~ 0.28) [43].

The overall structure of $[Mg(H_2O)_4][(VO)_2(PO_4)_2]$ may thus be described as layers of four-connected net of corner-sharing VO_5 square pyramids and phosphate PO_4 tetrahedron. Each VO_5 pyramid shares four basal O atoms with four different PO_4 groups. Along the [101] direction, the vanadyl O atoms alternately point up and down relative to the layer. Two neighboring layers are aligned to order the oxo-groups of the vanadyl sites directly towards

one another along the b-axis, and the two corresponding vanadyl(IV) oxo atoms are coordinated to an Mg atom in a trans fashion, such that a linear V group is formed (Fig. 3).

The distance between the [(VO)(PO_4)] planes, defined by the best planes through the O2 atoms, is 4.4785Å, which is comparable to a distance of 4.5230Å in [$Co(H_2O)_4$][$(VO)_2(PO_4)_2$] [42], 3.8570Å for $Zn_2VO(PO_4)_2$ [16] which may be compared to a distance of 3.91Å in vanadyl orthophosphate [$(VO(PO_4)_2$] [44]. Significantly, the orthovanadate structure consists of (VO6) octahedra and (PO_4) tetrahedra arranged in layers held together by long V-O bonds. Thus, in orthophosphate, the layers stack to orient the V=O vertices of one layer directly in line with the vacant sites of the (VO_5) units of the next layer, producing [V=O….V=O....V=O] chains of distorted [VO_6] octahedra. The registry of [$VO(PO_4)$] layers of title compound [$Mg(H_2O)_4VO_2(PO_4)_2$] is distinct from that of [$VO(PO_4)$] and related by one vanadium polyhedron to point the [V=O] vertices of adjacent layers at one another. The structure of [$Mg(H_2O)_4$][$VO(PO_4)]_2$ is thus related to that of [$VO(PO_4)$] by the expansion of the interlamellar spacing, translation of the layers relative to each other to provide a coordination sit for the Mg^{2+} cation and reduction of the vanadium sites to V(IV). The structural transformation requires only shearing of planes without disruption of any V-O-P bonds and suggests that [$Mg(H_2O)_4$][$VO(PO_4)]_2$ may be described as a reduced $VO(PO_4)_2$ phase with intercalated $[Mg(H_2O)_4]^{2+}$ units. The structure of [$Mg(H_2O)_4$][$VO(PO_4)]_2$ is quite distinct from that of $Ni_{0.5}[VOPO_4].1.5H_2O$ [45], a previously reported example of a nickel(II) and cobalt(II) vanadyl (IV) phosphate phases [46, 42]. In contrast to the structure of the title compound, $Ni_{0.5}[VOPO_4].1.5H_2O$ exhibits a three-dimensional architecture with channels to accommodate the aqua ligands of the NiO6 octahedron. Furthermore, the latter features the much more common octahedral V(IV) coordination sites with a [$V_2(\mu\text{-}O)(\mu_2\text{-}PO_4)_2$] structural motif. The adjacent layers are held in position by the $MgO_2(H_2O)_4$ octahedral pillars bonded to the P centers and V to complete the resulting 3-D architecture (Fig. 4a). Such connectivity

creates two intersecting 8-MR channels parallel to the [010] direction, into which the coordinated water molecules protrude. Both pore walls of the 8-MR channels are severely staggered, which leads to only six polyhedra visible in (Fig. 4a), and the opening of two 8-MR channels are built by two $MgO_2(H_2O)_4$, two PO_4 groups and four VO5 in the same sequence of $–MgO_2(H_2O)_4–VO_5–PO_4–VO_5–MgO_2(H_2O)_4–VO_5–PO_4–VO_5–$ in (Fig. 4b and 4c)

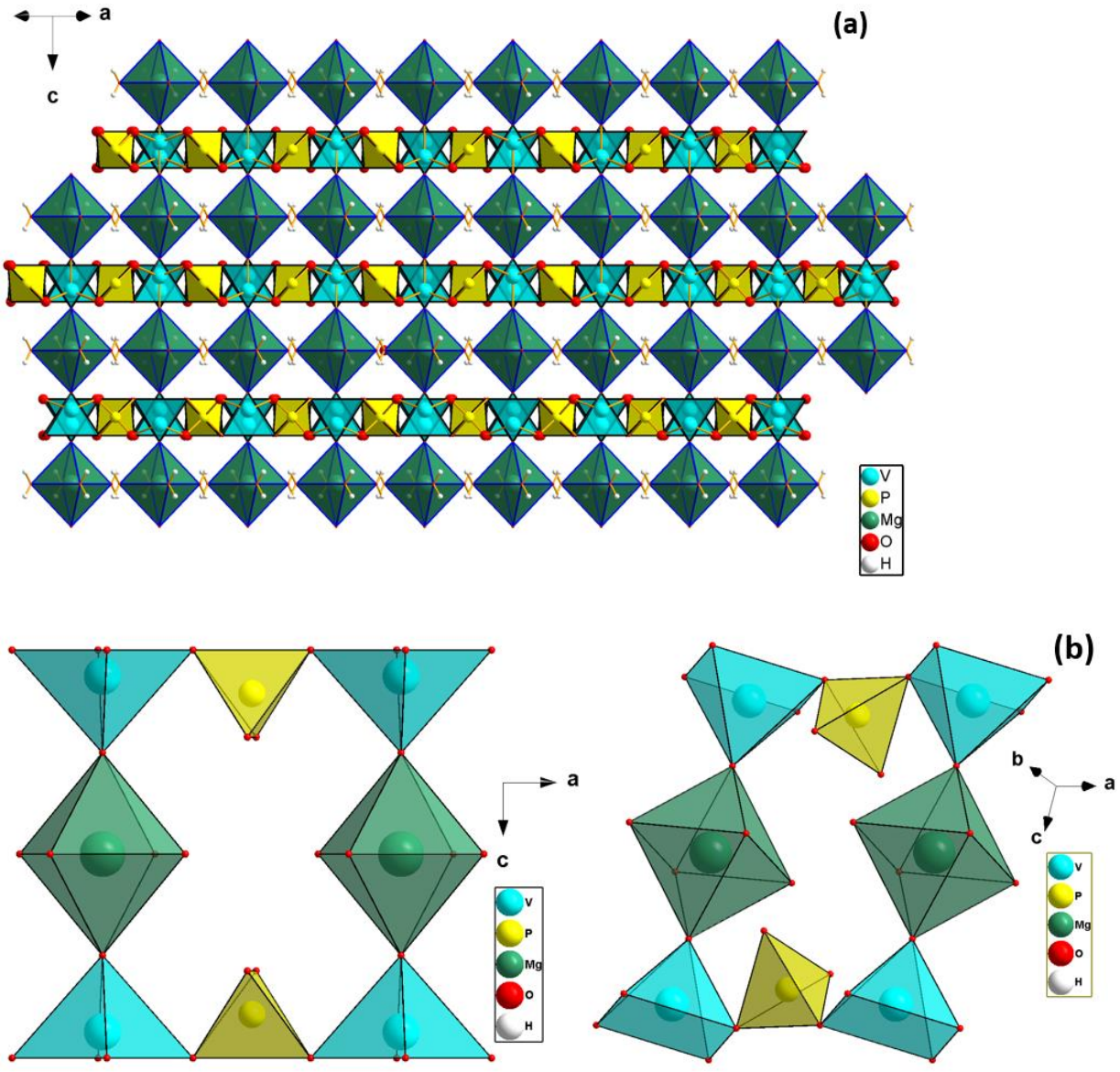

Fig. 4: (a) Polyhedral view of the 3-D framework of 1 along the [101] direction. (b) The 8-MR opening along the two directions.

4. Infrared spectroscopy and scanning electron microscopy (SEM)

We looked into the vibrational characteristics of vanadyl phosphate $[Mg(H_2O)_4][VO(PO_4)]_2$ to provide more details on the crystal structure. The presence of the phosphate group, vanadyl(IV) group, and water molecules were all identified using infrared spectroscopy. The designated infrared bands for $[Mg(H_2O)_4][VO(PO_4)]_2$ are listed in Table 4. The phosphate group, vanadyl(IV), and water can all be seen in compound 1's infrared spectrum as having different vibrational modes (Fig. 5). There are three significant bands present in the FT-IR spectrum, with wavelengths between 3600-2950 cm^{-1}, 1160-890 cm^{-1} and 600-400cm^{-1}. The deconvolution technique offers a thorough band-based interpretation. In line with the structure determined by single crystal X-ray structure, the FT-IR spectrum shows that the molecule contains all the functional groups. Even if assigning each band in detail is challenging, the most crucial attribution mode is obtained by comparison with comparable and related chemicals published in the literature [47-51], according to the previously reported IR spectroscopic description of some vibrational vanadyl phosphate. The strong bands at 958 cm^{-1} and 1039 cm^{-1} are due to the P-O symmetric stretching vibration in the group PO4 tetrahedrons and V-O-P stretching vibration, respectively [49, 50]. PO4 symmetric stretching overlapped with a P-O-V deformation band. This broadened band has the center of gravity in the same position at about 910 cm^{-1} in the present compound. The band at 988 cm^{-1} can be assigned to V=O stretching vibration, and the bands at 582 cm^{-1} and 542 cm^{-1} seem to be from the coupled V-O and P-O bending modes either in $[Mg(H_2O)_4][VO(PO_4)]_2$ [48,49]. Furthermore, we see the O-H stretching mode for coordinated water in the range of 2950-3600 cm^{-1} [52]. A band further supports the presence of the latter at 1640 cm^{-1}, which can be ascribed to the O-H bending vibration of water molecules. Finally, the band observed at 457 cm^{-1} corresponds to the stretching vibration of (Mg-O), similar to those found in the literature [53].

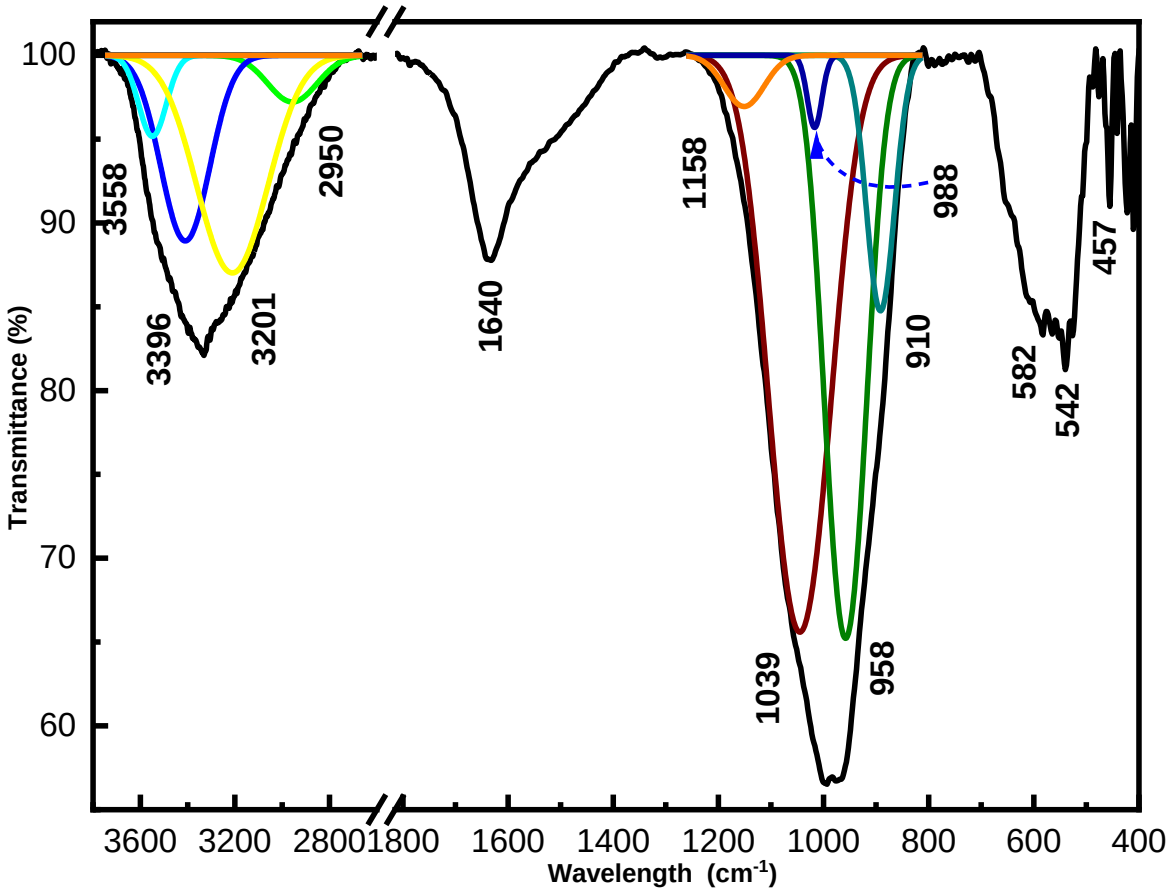

Fig. 5: Infrared spectrum of $[Mg(H_2O)_4][VO(PO_4)]_2$

Table 4: IR spectral data (cm^{-1}) and bands assignment for ($[Mg(H_2O)_4][VO(PO_4)]_2$.

Assignment	**Bands (cm^{-1})**
ν_s(V-O-P)	958
ν_s(P-O)	1039
ν_s (V=O)	988
δ(V-O)	582
δ(p-O)	542
ν_s(O-H)	2950-3600
δ(O-H)	1640
ν(Mg-O)	457

The scanning electron microscopy (SEM) image of the as-synthesized sample is shown in Fig. 6a and 6b. The sample comprises irregular particles ranging from ~10 to 1 μm, as observed in the SEM images. The chemical composition was analyzed by energy-dispersive X-ray

spectroscopy (EDX) in a selected particle area Fig 6(i-n). It can be seen that the elements of V, Mg, P, and O are distributed uniformly in the particle.

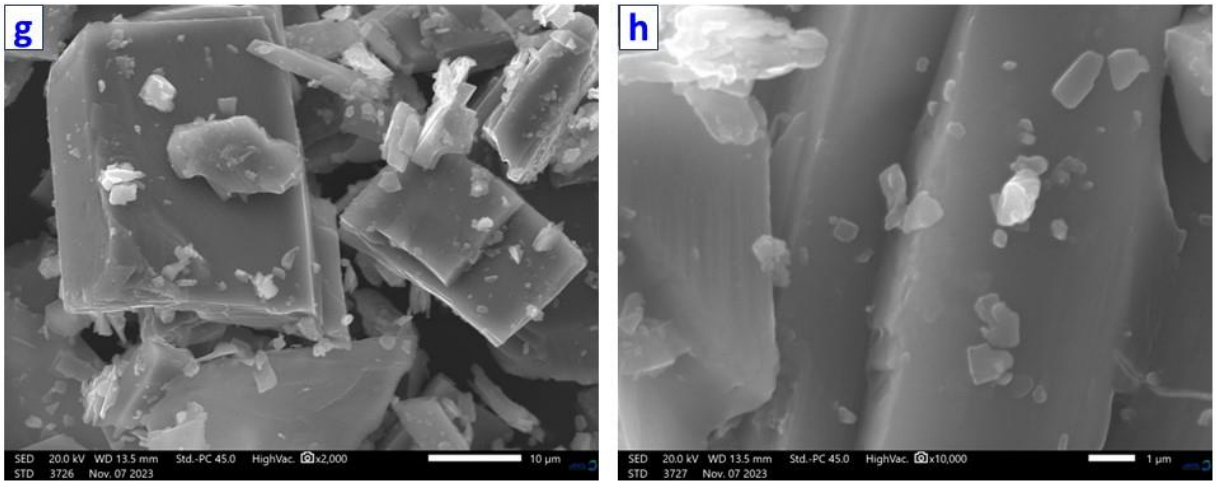

Fig. 6a: Typical SEM images at (g) low and (h) high magnification scanning Electron Microscope Micrographs of $[Mg(H_2O)_4][VO(PO_4)]_2$

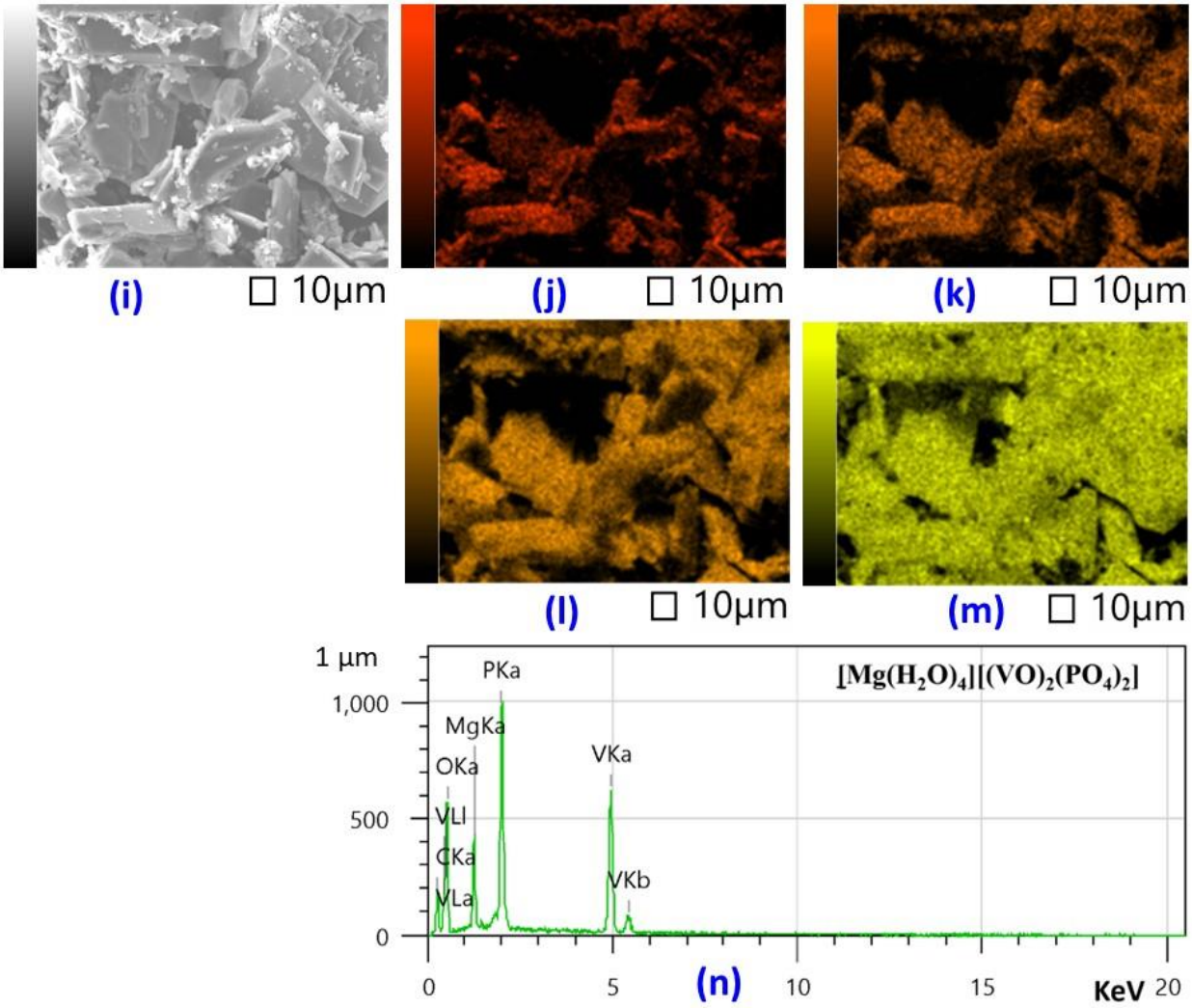

Fig. 6b: (i) Representative particles of as-synthesized samples and elemental mapping showing the uniform distribution of O(j), Mg(k), P(l), V(m) atoms. EDX spectrum, we capture signals of constituent elements (n).

5. Thermal Analysis *(TGA/DTA)*

Thermogravimetry (TG) measurements were carried out in dynamic air using a Diamond instrument (Perkin-Elmer) thermal analyzer. The treatment of this compound was realized in the flowing air (Debit= 50 mL/min) in the temperature range of 25-1000 °C (scan rate= 10°C/min), as shown in Fig. 7. The powdered sample was spread evenly in a large crucible to prevent the mass effect. The TGA curve (Fig. 7) shows the compound is thermally stable up to 200 °C. Subsequently, the weight loss occurs in two steps with a total weight loss of 15.5% between ≈200 and ≈500 °C, which corresponds to dehydration of the sample; this dehydration

is also seen in DTA by exothermic peaks at ≈250 and ≈450 °C. The observed total weight difference between room temperature and 500 °C is somewhat lower well with the calculated value for $[Mg(H_2O)_4][VO(PO_4)]_2$ (calcd/found = 17.13%/15.5%) showing water molecules loss in two steps near 250 and 400 °C. However, the four water molecules are crystallographically equivalent. The endothermic peak at ≈550 °C in the DTA and gain (1.2%) of the TG curve can be interpreted by a recrystallization reaction, which means that the structure formed between ≈180 and ≈550 °C is metastable and at higher temperatures transforms into $Mg(VO)_2(PO_4)_2$.

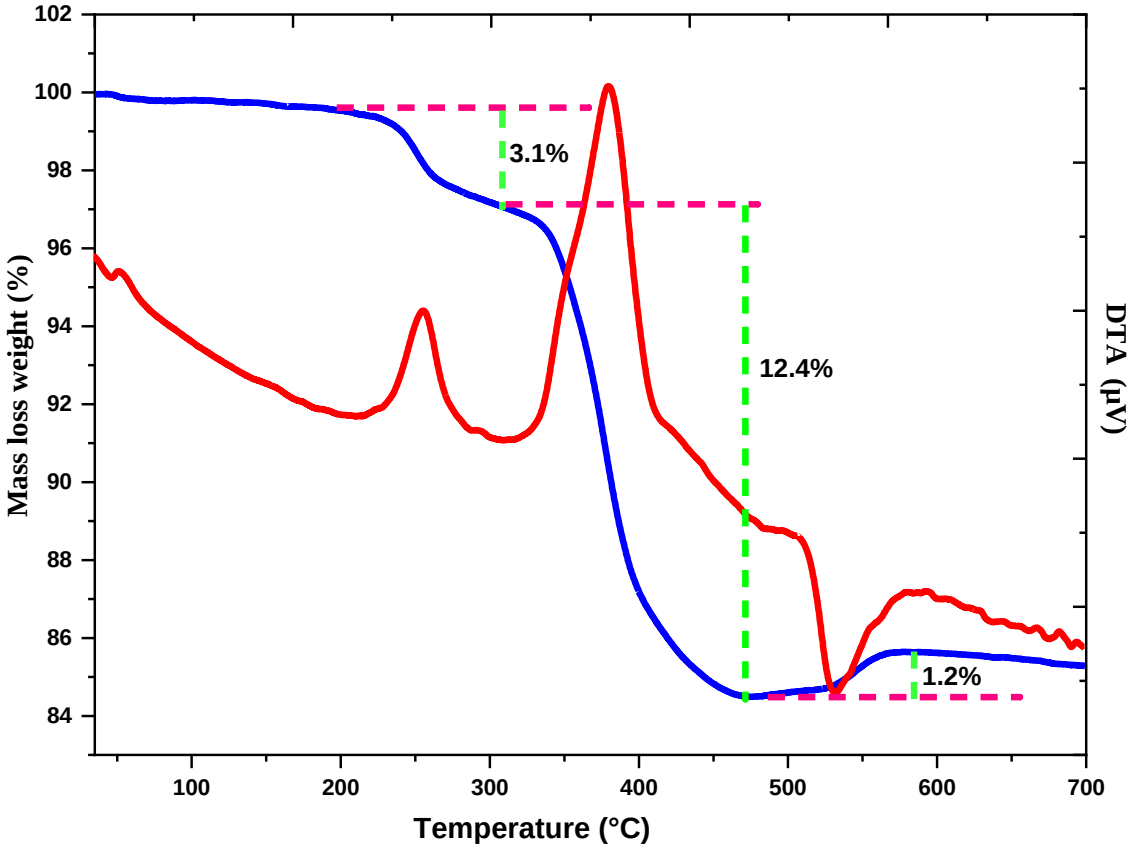

Fig. 7: TGA-DTA analyses of $[Mg(H_2O)_4][VO(PO_4)]_2$

6. Determination of catalytic reduction of nitrophenol isomers

Powder particles of the compound obtained from the grounded single crystals previously used for the structural determination are tested as a catalyst performance for the reduction reaction of three nitrophenol isomers (4-nitrophenol, 3-nitrophenol, and 2-nitrophenol) with sodium

tetrahydroborate $NaBH_4$. The results are presented in Fig. 8 (a-c). The vanadyl(IV) phosphate compound was very efficient as a catalyst. In fact, at the beginning stage, when we mixed the nitrophenol isomers with sodium tetrahydroborate, phenolate anions were produced, which caused a strong coloration of the solution. No reduction was detected with the activity of sodium tetrahydroborate alone for several days. However, after the addition of the powder particles of the compound, the solution becomes uncolored in a few seconds for all three-nitrophenol isomers. The highest bands of absorption located at 401, 393, and 415 nm and corresponding respectively to 4-nitrophenol, 3-nitrophenol, and 2-nitrophenol disappear in favor of new bands located at 317, 328, and 347 nm for the 4-aminophenol, 3-aminophenol, and 2-aminophenol, respectively. In fact, 30 seconds were necessary at room temperature to achieve the reaction with the appearance of the corresponding three aminophenol isomers. The obtained result exhibits the high catalytic performance of the synthesized Tetraaquomagnesium(II) Vanadyl(IV) Phosphate in the reduction reaction of the nitrophenol isomers related to the anterior research study discovered in the literature as mentioned in Table 5.

Table 5: Reduction of 4-NP 3-NP and 2-Np by Tetraaquomagnesium(II) Vanadyl(IV) Phosphate, a comparison of reaction time with known compounds.

Catalyst	**Concentration of NP (mol/L)**	**Reaction Time (sec)**	**Reference**
$[Mg(H_2O)_4][VO(PO_4)]_2$	4×10^{-4}	120 for 4-NP 30 for 3-NP 60 for 2-NP	This work
$(H_3dien)[Ni(NO_3)(C_2O_4)_2].2H_2O$	4×10^{-4}	30 for 4-NP 30 for 3-NP 30 for 2-NP	[38]
$(H_3dien)[Cu(NO_3)(C_2O_4)_2].2H_2O$	4×10^{-4}	60 for 4-NP 30 for 3-NP 60 for 2-NP	[39]

$(C_4H_{12}N_2)[Co(H_2O)_6](HPO_4)_2$	4×10^{-4}	240 for 4-NP 30 for 3-NP 240 for 2-NP	[53]
CuMoO4	4×10^{-4}	840 for 4-NP 360 for 3-NP 840 for 2-NP	[54]

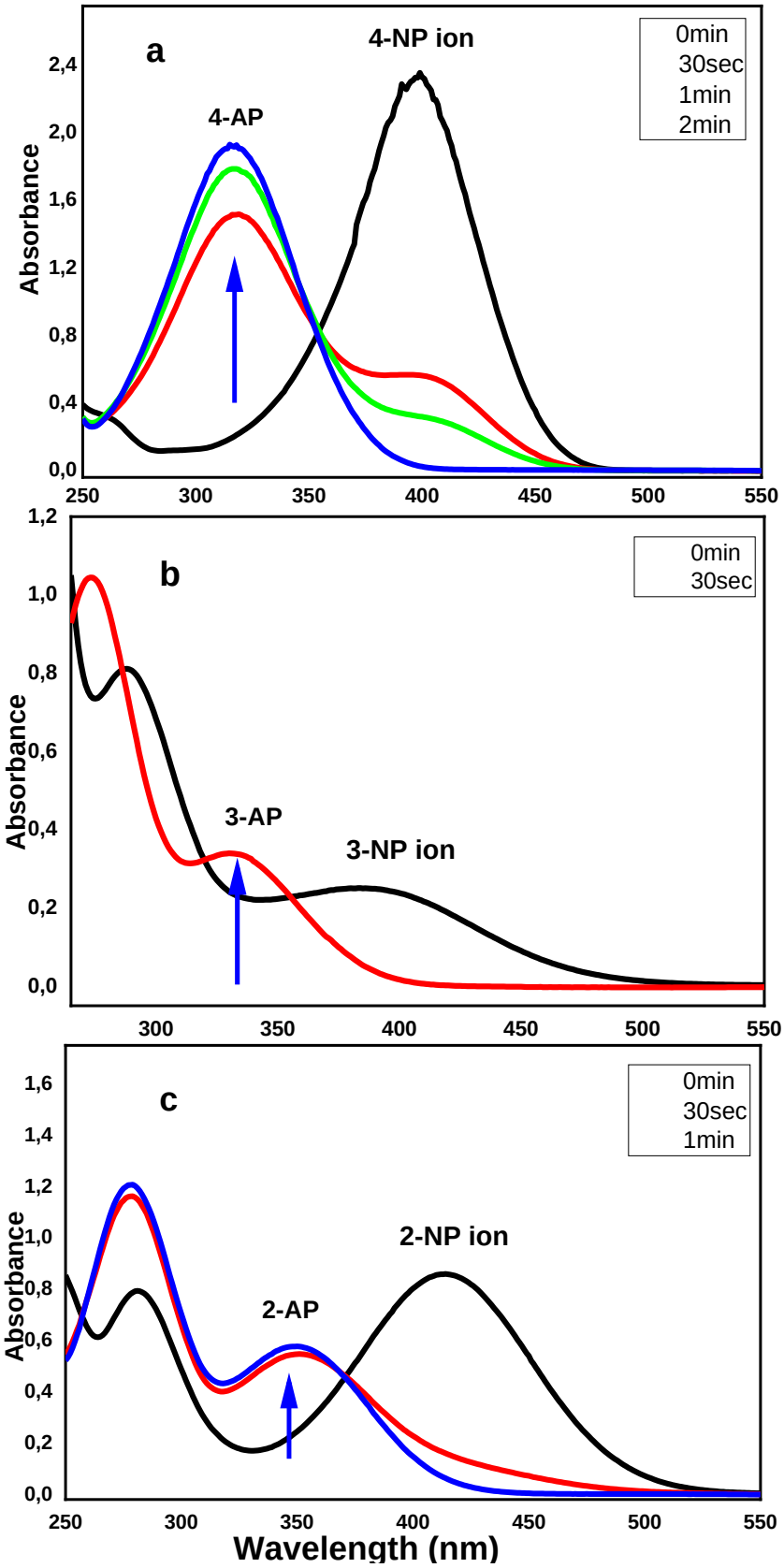

Fig. 8: UV-visible spectra of (a) 4-nitrophenol (4-NP), (b) 3-nitrophenol (3-NP), and (c) 2-nitrophenol (2-NP) isomers in the presence of sodium tetrahydroborate $NaBH_4$ and after adding $[Mg(H_2O)_4][VO(PO_4)]_2$ at room temperature.

3. Theoretical and computational results

3.1 Computational methods

In WIEN2k computations using the PBE-GGA approximation within the framework of density functional theory (DFT) [55-57], achieving energy convergence is an essential condition for obtaining reliable results. KPOINT, which represents the choice of K-points, significantly influences the discretization of the Brillouin zone in reciprocal space, impacting electronic state convergence models. The GMAX parameter, set at 12 $(a.u.)^{1-}$, establishes the upper limit of the energy cutoff in the plane-wave basis set, exerting a substantial effect on the completeness of the wavefunction representation. Equally crucial, the RKMAX parameter, set at 7, governs the maximum augmentation radius surrounding the atomic sites and plays an essential role in achieving convergence. In addition, the LMAX parameter, set at 10, dictates the highest angular momentum quantum number in the orbital basis set, thus influencing the accuracy of the description of electrons in various angular momentum states. Convergence of these parameters is essential to obtain electronic structure results that are accurate and physically meaningful. An important aspect of our investigation involves carefully sampling the Brillouin zone (BZ), for which we use the Monkhorst-Pack method [58] for discretization. In our density-of-state (DOS) computation, we opt for a 6×5×5 k-point grid, which facilitates a thorough exploration of electronic states within the material. Our computation rigor emphasizes achieving numerical convergence, which is considered accomplished when the total system energy reaches a tolerance level of 10^{-5} Ry.

3.2 Structural properties

$[Mg(H_2O)_4][VO(PO_4)]_2$ crystallizes in the Tetragonal (I4/m) space group. Mg^{2+} is coordinated to six O^{2-} atoms, forming MgO_6 octahedra that share corners with two VO_5 trigonal bipyramids. The Mg-O bond distances range from 2.08 to 2.12 Å. There are two distinct V^{4+} sites. In the first site, V^{4+} is linked to five O^{2-} atoms, creating distorted VO_5 trigonal

bipyramids. These share a corner with one MgO_6 octahedron and corners with four PO_4 tetrahedra. The V-O bond distances vary from 1.64 to 2.02 Å. In the second V^{4+} site, V^{4+} is connected to five O^{2-} atoms, forming distorted VO_5 trigonal bipyramids. These share a corner with one MgO_6 octahedron and corners with four PO_4 tetrahedra, exhibiting a 1° tilt in octahedral angles. One V-O bond is shorter (1.64 Å), and four are longer (2.01 Å). There are two P^{5+} sites. In the first, P^{5+} forms PO_4 tetrahedra bonded to four O^{2-} atoms, sharing corners with four VO_5 trigonal bipyramids. Three P-O bonds are shorter (1.55 Å), and one is longer (1.56 Å). In the second P^{5+} site, P^{5+} forms PO_4 tetrahedra, sharing corners with four VO_5 trigonal bipyramids, featuring two shorter (1.55 Å) and two longer (1.56 Å) P-O bonds. There are eight distinct H^+ sites. H^+ is singly bonded to O^{2-}in each, with H-O bond lengths ranging from 0.98 to 0.99 Å. Fourteen distinct O^{2-} sites exist, each exhibiting various bonding geometries and forming bonds with V^{4+}, P^{5+}, Mg^{2+}, and H^+ atoms (**Fig. 9**).

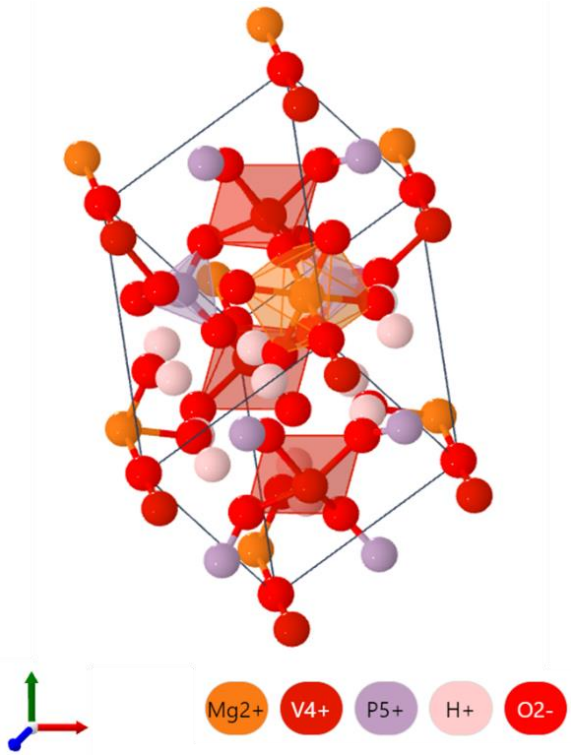

Fig. 9: $[Mg(H_2O)_4][(VO)_2(PO_4)_2]$ primitive cell crystallizes in the tetragonal I4/m space group.

3.3 Electronic properties

In this study, we conducted an extensive investigation into the electronic states within the valence band (VB) and conduction band (CB) of $[Mg(H_2O)_4][(VO)_2(PO_4)_2]$. Utilizing the PBE-GGA method, we precisely calculated band structures across an energy range from -10 eV to 15 eV. The results in Fig. 10 conclusively demonstrate that our compound exhibits an indirect bandgap with a computed value of 2.79 eV. This detailed exploration of the electronic band structure provides a fundamental grasp of the material's energy levels and transitions. It establishes a solid foundation for comprehensively analyzing its electronic and optoelectronic properties. Identifying the band gap in the band structure analysis highlights the material's potential for optoelectronic applications, wherein the direct nature of the band gap significantly influences its optical and electronic characteristics.

The exploration into the electronic structure of $[Mg(H_2O)_4][(VO)_2(PO_4)_2]$ reveals distinctive characteristics within both the valence and conduction bands. Symmetry analysis shows that the maximum valence band (MVB) and the minimum conduction band (MCB) precisely occur at symmetry points N and Γ, respectively. The total densities of states (TDOSs), presented in **Fig. 11**, exhibit a symmetrical profile along the x-axis, indicating the absence of ferrimagnetism or ferromagnetism purity states across valence and conduction bands. Moreover, the TDOSs highlight a discernible gap energy of 2.79 eV, consistent with the findings from the band structure analysis. This coherence deepens our understanding of the material's electronic characteristics, underscoring its potential for customized applications in electronics and optoelectronics.

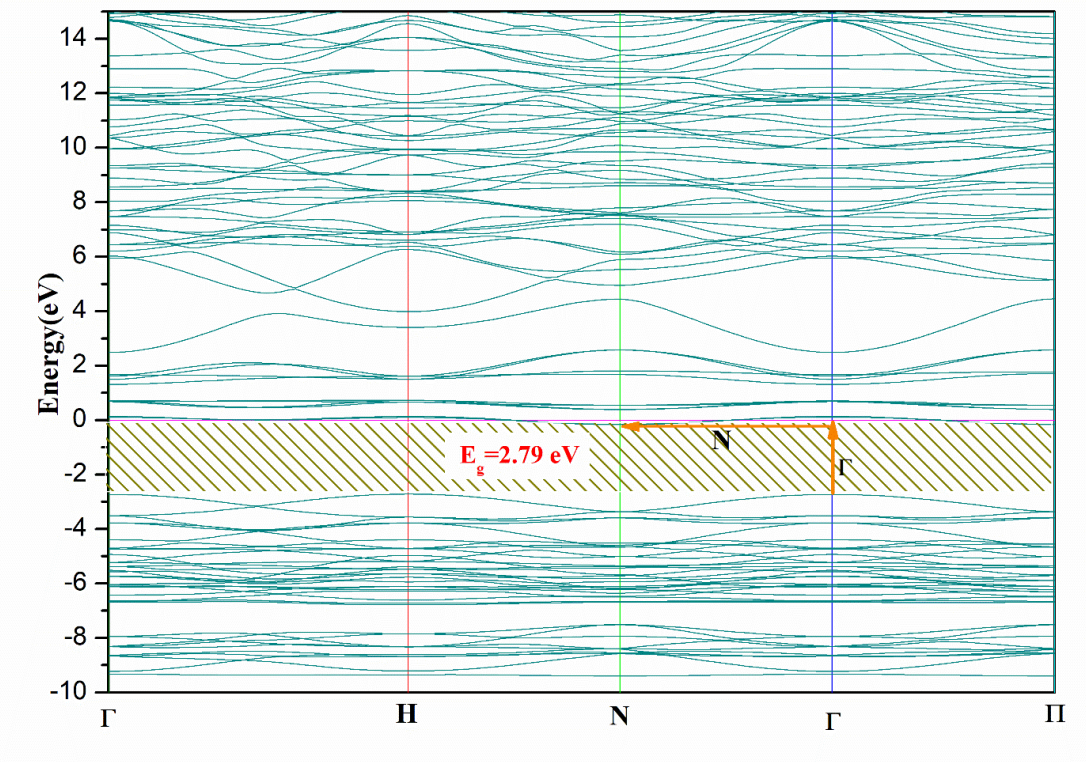

Fig. 10: Band structures along high-symmetry lines within the first Brillouin zone $[Mg(H_2O)_4][(VO)_2(PO_4)_2]$ calculated by PBE-GGA approximation.

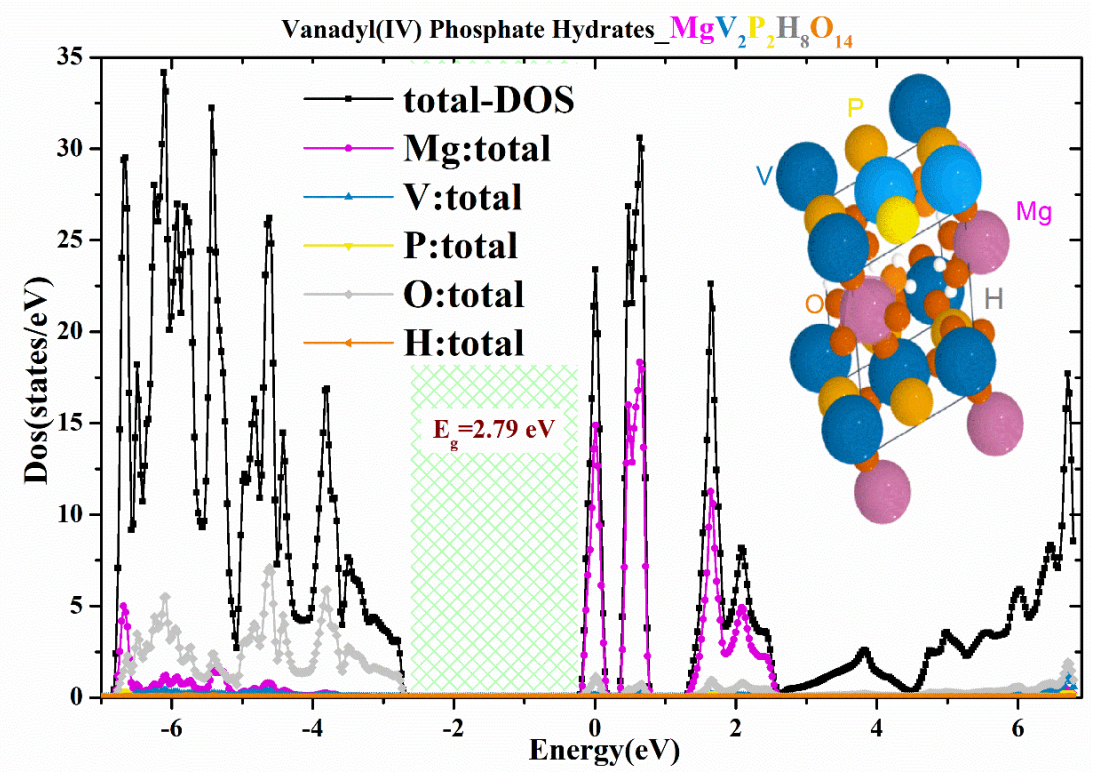

Fig. 11: The partial and total DOS of $[Mg(H_2O)_4][(VO)_2(PO_4)_2]$ calculated by PBE-GGA approximation.

Moreover, **Fig. 11** depicts a significant involvement of O-2p and Mg-3s orbitals in the valence band (VB). Interestingly, noticeable energy differences are observed between the O-2p and Mg-3s orbitals due to the elongated covalent bond lengths between these elements in the material's structure. Specifically, the formation of the maximum of the valence band (MVB) is considerably shaped by O-2p and Mg-3s orbitals. Conversely, the minimum of the conduction band (MCB) is markedly influenced by the same orbitals.

In-depth analyses of the partial density of states and band structures reveal an expansion in the valence band from -6.48 eV to 0 eV, utilizing the PBE-GGA approximation. The computed partial densities underscore the predominant contribution of O-2p and Mg-3s states in the valence band, with additional involvement of P-3p, V-3d, and H-1s states. In contrast, the conduction bands (CB) are primarily driven by O-2p states, including Mg-3s states. These findings highlight a noteworthy hybridization among different states within the material's electronic structure.

3.4 Optical properties

Our first step in investigating the optical properties is to compute the dielectric coefficient. Subsequently, we determine additional optical parameters using the equations outlined in the referenced source. The optical parameters obtained through the PBE_GGA approach are depicted in **Figs. 12-16** over the energy spectrum ranging from 0 to 10 eV.

Equation (1) represents the dielectric function [59]:

$$\varepsilon(\omega) = \varepsilon_1(\omega) + i\varepsilon_2(\omega) \quad (1)$$

In this context, $\varepsilon_1(\omega)$ and $\varepsilon_2(\omega)$ denote the real and imaginary components of the dielectric function, respectively. It is essential to highlight that $\varepsilon_1(\omega)$ is related to polarization and anomalous dispersion, whereas the value of $\varepsilon_2(\omega)$ is indicative of the energy dispersion within the medium.

Utilizing the dielectric function to analyze the optical properties of a material presents a convenient and flexible approach to investigating the interaction between light and materials. This encompasses the study of phenomena like light reflection, transmission, and absorption.

In the domain of electronic structure calculations, particularly those utilizing the PBE-GGA (Perdew-Burke-Ernzerhof Generalized Gradient Approximation), the absorption coefficient (α) can be calculated as a function of energy (eV). This computation, illustrated in **Fig. 12**, helps elucidate a material's absorption characteristics. The absorption coefficient serves as a metric for gauging how efficiently a material absorbs light across different wavelengths and is derived from the imaginary component of the dielectric function (ε) (refer to Eq 2) [60].

$$\alpha(\omega) = \sqrt{2\left(\sqrt{\varepsilon_1(\omega)^2 + \varepsilon_2(\omega)^2} - \varepsilon_1(\omega)\right)} \quad (2)$$

In **Fig. 12**, a notable feature is the minimal absorption coefficient observed in the visible and infrared spectra. This suggests that the material has a low propensity for absorbing light within these wavelength ranges, indicating that light can effectively traverse through the material in these regions. The transparency to visible and infrared light implies that the material may have specific optical properties desirable for applications where light transmission is essential.

Contrastingly, the UV range of the spectrum exhibits multiple peaks in the absorption coefficient graph. These peaks signify the material's enhanced capacity to absorb light in ultraviolet. This heightened absorption suggests that the material may be exceptionally responsive to ultraviolet radiation, which can affect various applications such as sensors, photodetectors, or other technologies reliant on UV light absorption.

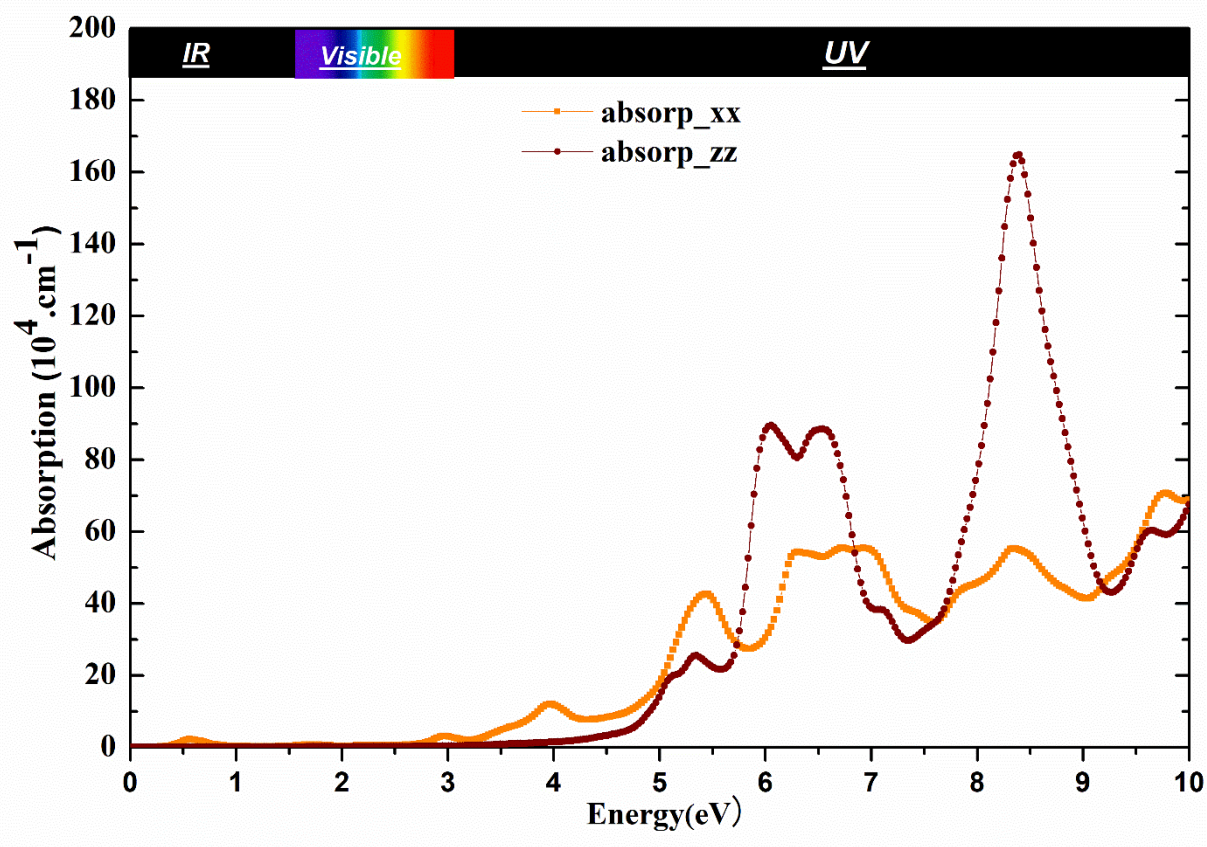

Fig. 12: The Absorption coefficient of **$[Mg(H_2O)_4][(VO)_2(PO_4)_2]$]** calculated by PBE-GGA approximation.

The optical conductivity (σ) is linked to the imaginary part of the dielectric function (ε) by the relationship defined in Equation 3:

$$\sigma(\omega)=\frac{\omega\varepsilon_1(\omega)}{4\pi} \quad (3)$$

As depicted in Fig. 13, optical conductivity is a fundamental parameter in examining materials' optical properties, especially within electromagnetic interactions. It defines the material's capability to conduct electric current in reaction to light absorption. This conductivity is intricately connected to the material's electronic structure and dynamic responsiveness to incident electromagnetic fields. The insights gained from optical conductivity analysis are pivotal for understanding how materials interact with light and can have broad implications for developing various optical and electronic devices.

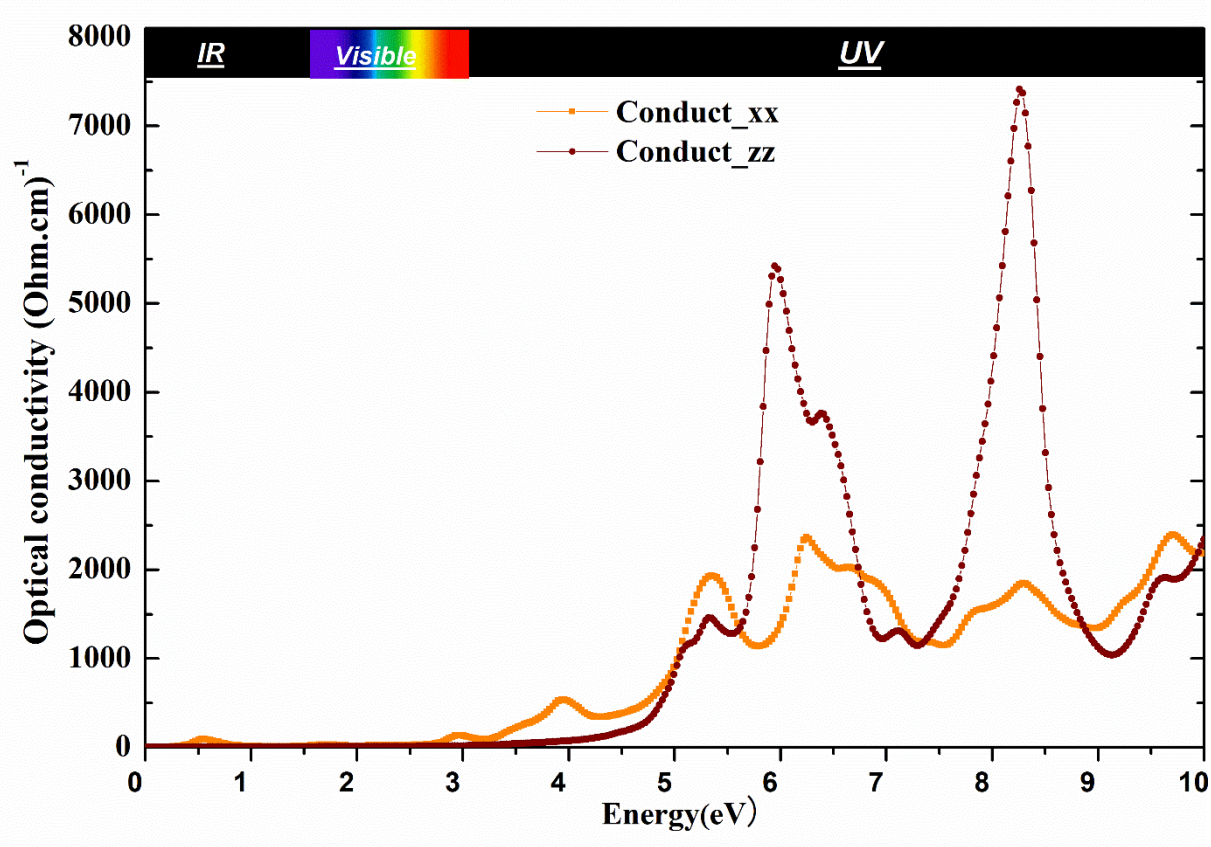

Fig. 13: The Optical conductivity of **$[Mg(H_2O)_4][(VO)_2(PO_4)_2]$** calculated by PBE-GGA approximation.

Equation (4) articulates the connection between the real and imaginary components of the dielectric function and the refractive index of the material

$$n(\omega) = \sqrt{\frac{\sqrt{\varepsilon_1(\omega)^2 + \varepsilon_2(\omega)^2} + \varepsilon_1(\omega)}{2}} \qquad (4)$$

It is defined as the correlation between the speed of light in a vacuum and the speed of light within a material. A material with a higher refractive index deviates light more than one with a lower refractive index. As illustrated in **Fig. 14**, the refractive index exhibits a substantial value in the low-energy region, approximately around 1.7 at zero frequency, with a noticeable increase observed in the high-energy region. It then decreases in the UV region.

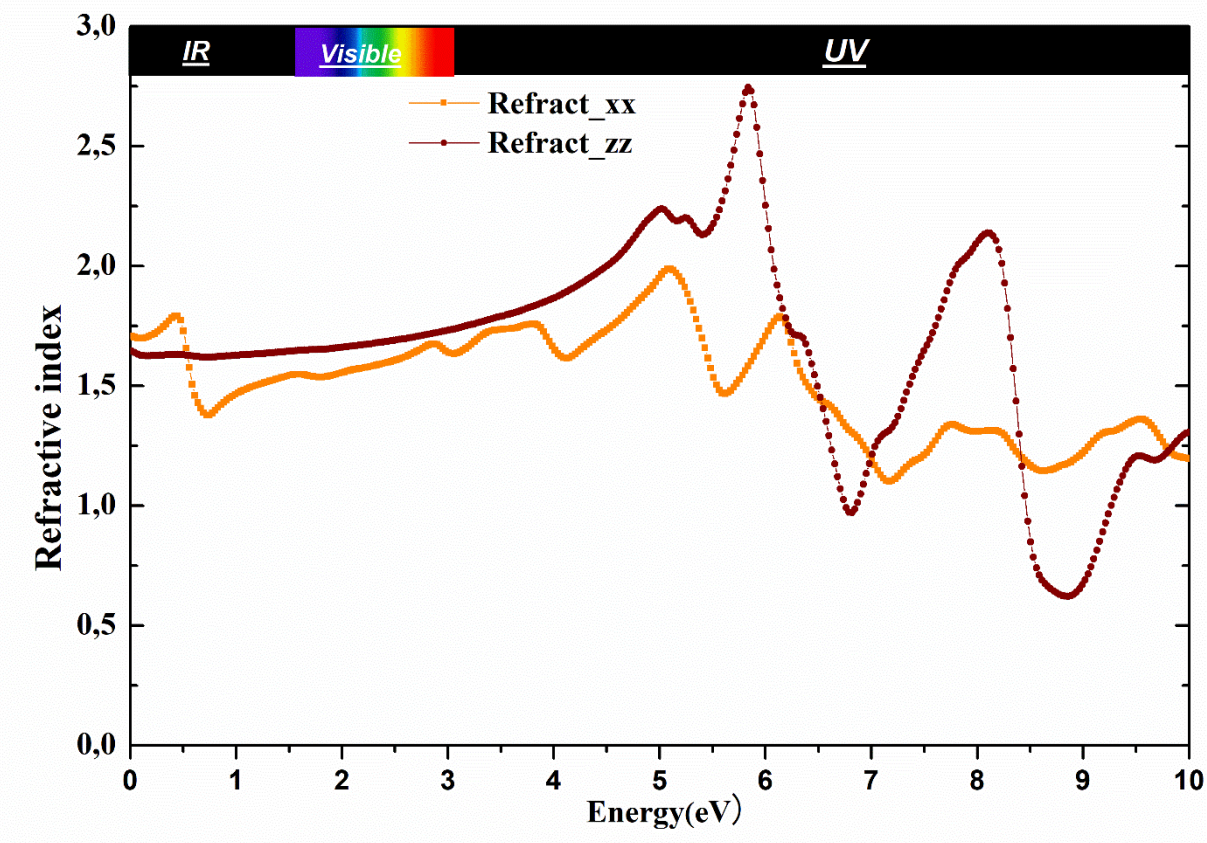

Fig. 14: The Refractive index of **$[Mg(H_2O)_4][(VO)_2(PO_4)_2]$** calculated by PBE-GGA approximation.

The imaginary part of the dielectric function is related to the extinction coefficient by the equation (5):

$$k(\omega) = \sqrt{\frac{\sqrt{\varepsilon_1(\omega)^2 + \varepsilon_2(\omega)^2} - \varepsilon_1(\omega)}{2}} \qquad (5)$$

The extinction coefficient measures how much a material absorbs light at different wavelengths. It is directly related to the absorption coefficient, providing a more intuitive understanding of light absorption in a material. As shown in **Fig. 15**, the extinction coefficient increases with higher energy, reaching elevated values in the Ultraviolet range for both parallel and perpendicular components within the PBE-GGA approximations (see **Fig. 15**).

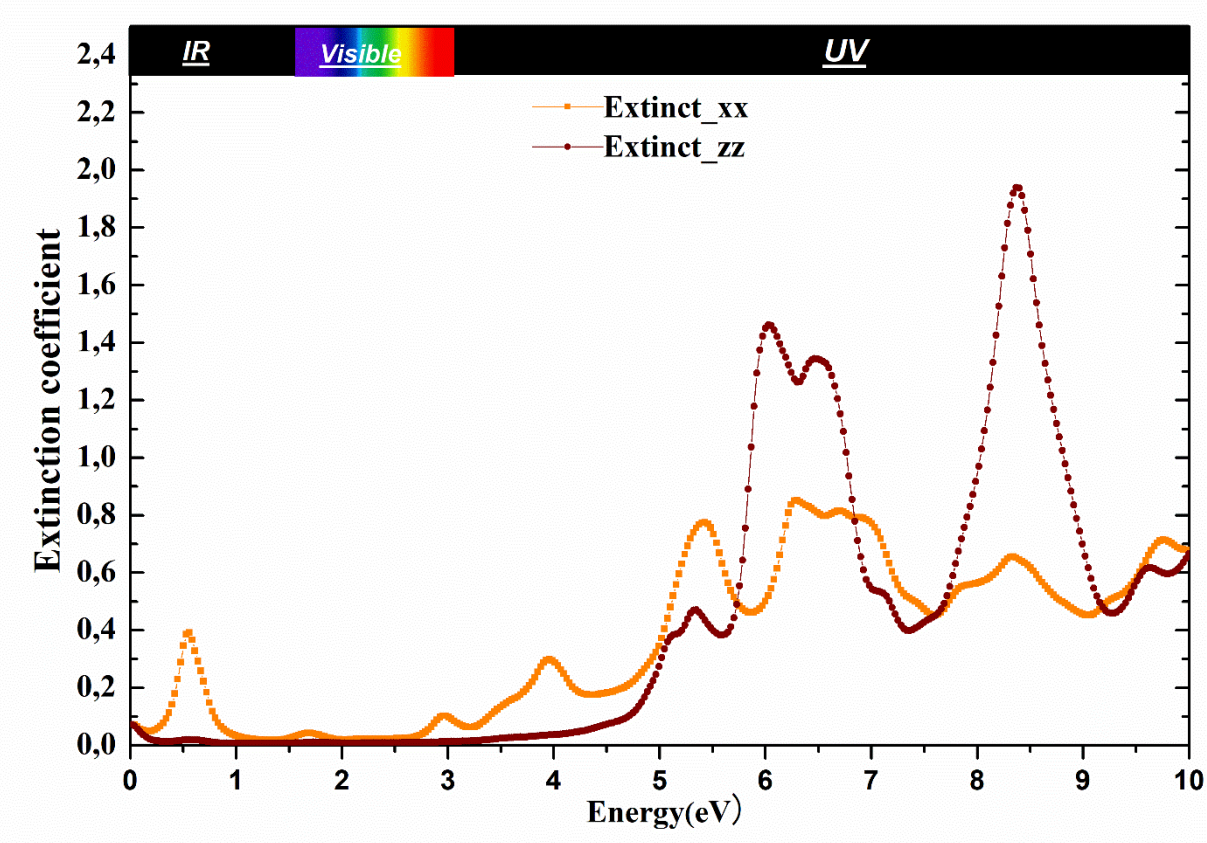

Fig. 15: The Extinction coefficient of **$[Mg(H_2O)_4][(VO)_2(PO_4)_2]$** calculated by PBE-GGA approximation.

Reflectivity represents the fraction of incident light that a material reflects at a specific wavelength. This value can be determined by utilizing the refractive index (refer to Eq 6) [61]:

$$R(\omega) = \left| \frac{\sqrt{\varepsilon_1(\omega) + j\varepsilon_2(\omega)} - 1}{\sqrt{\varepsilon_1(\omega) + j\varepsilon_2(\omega)} + 1} \right|^2 \quad (6)$$

The coefficient of light reflectivity serves as a pivotal parameter in optical analysis, encapsulating the intricate interplay of dielectric functions. This coefficient is commonly defined as the ratio of light energy reflected at the semiconductor surface, providing valuable insights into the material's interaction with incident light.

As shown in Fig. 16, the optical reflectivity within the visible range at zero frequencies remains consistently below 6%. This observation signifies that the material exhibits a

relatively low reflectivity in the visible spectrum, implying that a significant portion of incident light is transmitted or absorbed rather than reflected. A low reflectivity in the visible range may be advantageous for applications where minimizing light reflection is desirable, such as in optical coatings or devices aimed at maximizing light transmission.

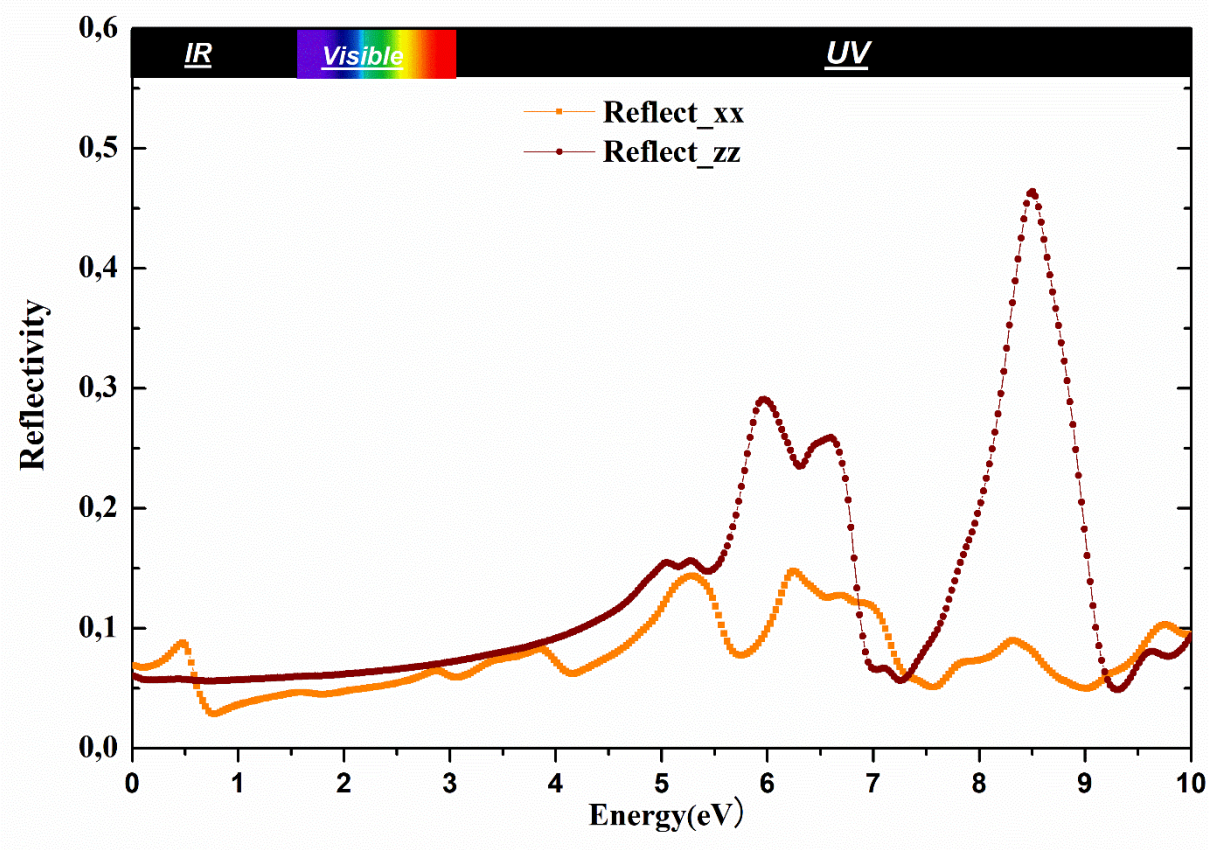

Fig. 16: The Reflectivity of **$[Mg(H_2O)_4][(VO)_2(PO_4)_2]$** calculated by PBE-GGA approximation.

Conclusions

In summary, we have examined diverse properties of vanadyl(IV) phosphate hydrates using a hydrothermal synthesis approach and DFT calculations. The experimental synthesis of these novel vanadyl(IV) phosphate hydrates has revealed a fascinating structure. Its structure consists of $MgO_2(H_2O)_4$ octahedra to form an entire 3-D framework structure containing two intercrossing 8-MR channels occluded by the coordinated water molecules. It is shown that a mild hydrothermal route can facilitate the self-assembly of polymetallic oxide materials. Studies on analogous polymetallic phosphate compounds of different combinations of metal ions are in progress. The phase purity of the compound was confirmed by powder XRD measurement. The thermal behaviors of the vanadyl(IV) phosphate hydrates were investigated. Moreover, the morphology and the size of the two nickel complexes were monitored by scanning electron microscopy (SEM). DFT calculations show significant hybridization between the Mg-3s and O-2p states in both the valence and conduction bands. Additionally, an interesting bandgap is identified with a value of 2.79 eV.

Acknowledgment

A. Soussi thanks the research team on Energies and Sustainable Development High School (Ibn Zohr University, Agadir, Morocco) for the WIEN2k computations calculations access. He is also grateful to Prof. P. Blaha and Prof. K. Schwarz at Wien Technical University for the Wien2k code and their kind reply. He also

References

[1] M.S. Kishore, V. Pralong, V. Caignaert, S. Malo, S. Hebert, U.V. Varadaraju, B. Raveau, Topotactic insertion of lithium in the layered structure $Li_4VO(PO_4)_2$: The tunnel structure $Li_5VO(PO_4)_2$. *J. Solid State Chem, 181 (2008)* 976-982. https://doi.org/10.1016/j.jssc.2008.01.044

[2] M.S. Kishore, V. Pralong, V. Caignaert, U.V. Varadaraju, B. Raveau, Synthesis and electrochemical properties of a new vanadyl phosphate: $Li_4VO(PO_4)_2$. *Electrochem. Commun, 8* (2006) 1558-1562. https://doi.org/10.1016/j.elecom.2006.07.028

[3] A.S. Hameed, M.V. Reddy, B.V.R. Chowdari, J.J. Vittal, Carbon coated $Li_3V_2(PO_4)_3$ from the single-source precursor, $Li_2(VO)_2(HPO_4)_2(C_2O_4)\cdot 6H_2O$ as cathode and anode materials for Lithium ion batteries. *Electrochimica Acta, 128* (2014) 184-191. https://doi.org/10.1016/j.electacta.2013.10.189

[4] J. Song, M. Xu, L. Wang, J.B. Goodenough, Exploration of $NaVOPO_4$ as a cathode for a Na-ion battery. *Chem comm, 49 (2013)* 5280-5282. https://doi.org/10.1039/c3cc42172d

[5] Z. Mao, R. Wang, B. He, Y. Gong, H. Wang, Large-Area, Uniform, Aligned arrays of $Na_3(VO)_2(PO_4)_2F$ on carbon nanofiber for quasi-solid-state Sodium-Ion hybrid capacitors. *Small, 15* (2019) 1902466. https://doi.org/10.1002/smll.201902466

[6] G. Deng, D. Chao, Y. Guo, Z. Chen, H. Wang, S.V. Savilov, J. Lin, Z.X. Shen, Graphene quantum dots-shielded $Na_3(VO)_2(PO_4)_2F$@C nanocuboids as robust cathode for Na-ion battery. *Energy Storage Materials, 5*(2016) 198-204. https://doi.org/10.1016/j.ensm.2016.07.007

[7] S. Ezzine Yahmed, M. Ayed, M.F. Zid, A. Driss, β-$K(VO_2)_2(PO_4)$. *Acta Crystallogr. E: Crystallogr. Commun, 69 (2013)* i2-i2. https://doi.org/10.1107/S1600536812049884

[8] I.V. Tereshchenko, D.A. Aksyonov, A. Zhugayevych, E.V. Antipov, A.M. Abakumov, Reversible electrochemical potassium deintercalation from> 4 V positive electrode material $K_6(VO)_2(V_2O_3)_2(PO_4)_4(P_2O_7)$. *Solid State Ion, 357 (2020)* 115468. https://doi.org/10.1016/j.ssi.2020.115468

[9] K.H. Lee, Y.W. Lee, S.W. Lee, J.S.Ha, S.S.Lee, J.G. Son, Ice-templated self-assembly of $VOPO_4$-graphene nanocomposites for vertically porous 3D supercapacitor electrodes. *Scientific reports, 5 (2015)* 1-10. https://doi.org/10.1038/srep13696 (2015)

[10] A. Khan, A.A.P. Khan, M.M. Rahman, A.M. Asiri, High-performance polyaniline/vanadyl phosphate (PANI-$VOPO_4$) nanocomposite sheets prepared by exfoliation/intercalation method for sensing applications. *European Polymer Journal, 75 (2016)* 388-398.https://doi.org/10.1016/j.eurpolymj.2016.01.003

[11] J. Li, Y. Qi, F. Xiao, S. Bao, M. Xu, A facilely-synthesized polyanionic cathode with impressive long-term cycling stability for sodium-ion batteries. *Chem comm, 57 (2021)* 9566-9569. https://doi.org/10.1039/D1CC02203B

[12] M.A. Deyab, B. El Bali, Q. Mohsen, R. Essehli, Design new epoxy nanocomposite coatings based on metal vanadium oxy-phosphate $M_{0.5}VOPO_4$ for anti-corrosion applications. *Scientific Reports, 11 (2021)* 1-8. https://doi.org/10.1038/s41598-021-87567-3

[13] S. Boudin, A. Guesdon, A. Leclaire, M.M. Borel, Review on vanadium phosphates with mono and divalent metallic cations: syntheses, structural relationships and classification, properties. Int. j. inorg. Mater, 2 (2000) 561-579. https://doi.org/10.1016/S1466-6049(00)00074-X

[14] S.L. Tey, M.V. Reddy, G.V. Subba Rao, B.V.R. Chowdari, J. Yi, J. Ding, J.J. Vittal, Synthesis, Structure, and Magnetic Properties of $[Li(H_2O)M(N_2H_3CO_2)_3]\cdot 0.5H_2O$ (M = Co,Ni) as Single Precursors to LiMO2 Battery Materials, Chem. Mater, 18 (2006) 1587–1594. https://doi.org/10.1021/cm0523891

[15] T.J. Boyle, M.A. Rodriguez, D. Ingersoll, T.J. Headley, S.D. Bunge, D.M. Pedrotty, S.M. De'Angeli, S.C. Vick, H. Fan, A Novel Family of Structurally Characterized Lithium Cobalt Double Aryloxides and the Nanoparticles and Thin Films Generated Therefrom, Chem. Mater, 15 (2003) 3903–3912. https://doi.org/10.1021/cm020902u

[16] Lii, K.H., & Tsai, H.J. (1991). Synthesis and crystal structure of $Zn_2VO(PO_4)_2$, a vanadyl (IV) orthophosphate containing a dimer of edge-sharing ZnO5 square pyramids. *J. Solid State Chem*, *90*(2), 291-295. https://doi.org/10.1016/0022-4596(91)90145-8

[17] Mar, A., Leroux, F., Guyomard, D., Verbaere, A., & Piffard, Y. Hydrothermal Synthesis and Structure of $Mn_2VO(PO_4)_2\cdot H_2O$. *J. Solid State Chem*, *115* (1995) 76-82. https://doi.org/10.1006/jssc.1995.1104

[18] C. Wadewitz, H. Müller-Buschbaum, Synthese und Struktureines Strontium-Vanadyl-Phosphats: $Sr_2(VO)(PO_4)_2$ /Synthesis and Structure of a Strontium Vanadyl Phosphate: $Sr_2(VO)(PO_4)_2$. *Zeitschrift für Naturforschung B, 51* (1996). 929-933. https://doi.org/10.1515/znb-1996-0705

[19] R.V. Shpanchenko, E.E. Kaul, C. Geibel, E.V. Antipov, The new lead vanadylphosphate $Pb_2VO(PO_4)_2$. *Acta Crystallogr. C Struct. Chem*, *62* (2006) i88-i90. https://doi.org/10.1107/s0108270106021597

[20] M. Skoulatos, J.P. Goff, N. Shannon, E.E. Kaul, C. Geibel, A.P. Murani, M. Enderle, A.R. Wildes, Spin correlations in the frustrated square lattice $Pb_2VO(PO_4)_2$. *J. Magn. Magn. Mater*, *310* (2007) 1257-1259. https://doi.org/10.1016/j.jmmm.2006.10.379

[21] E. E. Kaul, Ph.D. thesis, Technical University Dresden, 2005. Electronic version available at: http://hsss.slub-dresden.de/documents/1131439690937-4924/11314396
[22] R. Nath, A. A. Tsirlin, H. Rosner, and C. Geibel, Magnetic properties of $BaCdVO(PO_4)_2$: A strongly frustrated spin-1/2 square lattice close to the quantum critical regime, Phys. Rev. B 78 (2008) 064422. https://doi.org/10.1103/PhysRevB.78.064422
[23] R. Nath, A.A. Tsirlin, H. Rosner, C. Geibel, Magnetic properties of $BaCdVO(PO_4)_2$: A strongly frustrated spin-1 2 square lattice close to the quantum critical regime. *Physical Review B, 78* (2008) 064422. https://doi.org/10.1103/PhysRevB.78.064422
[24] A.A. Tsirlin, R. Nath, A.M. Abakumov, R.V. Shpanchenko, C. Geibel, H. Rosner, Frustrated square lattice with spatial anisotropy: Crystal structure and magnetic properties of $PbZnVO(PO_4)_2$. *Physical Review B, 81 (2010)* 174424. https://doi.org/10.1103/PhysRevB.81.174424
[25] H. Rosner, R.R.P. Singh, W.H. Zheng, J. Oitmaa, S.-L.Drechsler, and W.E. Pickett, Realization of a Large J_2 Quasi-2D Spin-Half Heisenberg System: Li_2VOSiO_4, Phys. Rev. Lett. 88 (2002) 186405. https://doi.org/10.1103/PhysRevLett.88.186405
[26] R. Melzi, P. Carretta, A. Lascialfari, M. Mambrini, M. Troyer,P. Millet, and F. Mila, $Li_2VO(Si,Ge)O_4$, a Prototype of a Two-Dimensional Frustrated Quantum Heisenberg Antiferromagnet, Phys. Rev. Lett. 85 1318 (2000). https://doi.org/10.1103/PhysRevLett.85.1318
[27] R. Melzi, S. Aldrovandi, F. Tedoldi, P. Carretta, P. Millet, and F. Mila, Magnetic and thermodynamic properties of Li_2VOSiO_4: A two-dimensional S=1/2 frustrated antiferromagnet on a square lattice, Phys. Rev. B 64, (2001) 024409. https://doi.org/10.1103/PhysRevB.64.024409
[28] E. E. Kaul, Ph.D. Dissertation, Technical University Dresden,2005.
[29] M. Weil, The struvite-type compounds $M[Mg(H_2O)_6](XO_4)$, where M= Rb, Tl and X= P, As. *Crystal Research and Technology: Cryst. Res. Technol, 43 (2008)* 1286-1291. https://doi.org/10.1002/crat.200800403
[30] H.Y. Kang, W.C.Lee, S.L. Wang, K.H. Lii, Hydrothermal synthesis and structural characterization of four layered vanadyl (IV) phosphate hydrates $A(VO)_2(PO_4)_2$. Cntdot. $4H_2O$ (A= Co, Ca, Sr, Pb). *Inorganic Chemistry, 31 (1992)* 4743-4748. https://doi.org/10.1021/ic00049a007
[31] O.V. Yakubovich, I.M. Steele, O.V. Dimitrova, A new type of mixed anionic framework in microporous rubidium copper vanadyl (V) phosphate, $Rb_2Cu(VO_2)_2(PO_4)_2$. *Acta crystallogr., C Struct. chem, 64 (2008)* i62-i65. https://doi.org/10.1107/S0108270108016454

[32] E. Boivin, J.N. Chotard, T. Bamine, D. Carlier, P. Serras, V. Palomares, T. Rojo, A. Iadecola, L. Dupont, L. Bourgeois, F. Fauth, C. Masquelier. L. Croguennec, Vanadyl-type defects in Tavorite-like $NaVPO_4F$: from the average long range structure to local environments. *J. Mater. Chem. A*, 5 (2017) 25044-25055 https://doi.org/10.1039/C7TA08733K

[33] P. Serras, V. Palomares, P. Kubiak, L. Lezama, T. Rojo, Enhanced electrochemical performance of vanadyl (IV) $Na_3(VO)_2(PO_4)_2F$ by ex-situ carbon coating. *Electrochemistry communications, 34 (2013)* 344-347. https://doi.org/10.1016/j.elecom.2013.07.010

[34] M. Akouibaa, I. Lakkab, A. Direm, M. Lachkar, R. Ouarsal, S. Rakib, V. Nasif, K. Sayin, N. Morley, B. El Bali, $[Cu_2(ox)(dien)_2](NO_3)_3$, a precursor for preparation of CuO nanoparticles: synthesis, structural, Hirshfeld surface analyses, and physico-chemical investigations. J. Mol. Struct. 1282 (2023) 135258 https://doi.org/10.1016/j.molstruc.2023.135258

[34] Rigaku Oxford Diffraction. CrysAlis CCD and CrysAlis RED. (*Versions 1.171.39.46*)], (2018).

[35] G.M. Sheldrick, SHELXT-Integrated space-group and crystal-structure determination. Acta Crystallogr. A. C71 (2015) 3-8. https://doi.org/10.1107/S2053273314026370

[36] L.J. Farrugia, WinGX suite for small-molecule single-crystal crystallography. J. Appl. Crystallogr. 32 (1999) 837-838. https://doi.org/10.1107/S0021889899006020

[37] K. Brandenburg K, H. Putz. Crystal Impact GbR, Postfach 1251, D 53002 Bonn, (2005) Germany.

[38] M. Akouibaa, H.O. Hassani, R. Ouarsal, S. Rakib, M. Lachkar, M. Poupon, M. Dusek, N. Morley, B. El Bali, $(H_3dien)[Ni(NO_3)(C_2O_4)_2].2H_2O$: Synthesis, crystal structure, catalytic activity and magnetic study. Chem. Data Collect. 2022 (42) 100969. https://doi.org/10.1016/j.cdc.2022.100969

[39] M. Akouibaa, M. Kadiri, M. Driouch, K. Tanji, R. Ouarsal, S. Rakib, M. Sfaira, N. Morley, M. Lachkar, B. El Bali, A. Zarrouk, El-E. Bendeif, Synthesis, catalytic activity, magnetic study and anticorrosive activity of mild steel in HCl 1 M medium of $(H_3dien)[Cu(NO_3)(C_2O_4)_2].2H_2O$. A redetermination at 100 K. Mater. Chem. Phys. 2023 (307) 128-130. https://doi.org/10.1016/j.matchemphys.2023.128130

[40] I.D. Brown, & D. Altermatt, Bond-valence parameters obtained from a systematic analysis of the inorganic crystal structure database. Acta Cryst. B41 (1985). 244-247. https://doi.org/10.1107/S0108768185002063

[41] B.Z. Lin, X.K. Pei, P.D. Liu, Tetraaquacobalt (II) bis [vanadyl (IV) phosphate], $[Co(H_2O)_4][VO(PO_4)]_2$. *Acta crystallogr., C Struct. chem, 59 (2003)* i97-i99. https://doi.org/10.1107/S0108270103017219

[42] E. Le Fur, J.Y. Pivan, Synthesis and crystal structure of the new zinc–magnesium vanadium (IV) phosphate hydrate $Mg_{(1-x)}Zn_x(VOPO_4)_2 \cdot 4H_2O$ (x∼0.28). *Materials research bulletin, 34 (1999)* 1117-1127. https://doi.org/10.1016/S0025-5408(99)00096-3

[43] F. Cavani, G. Centi, F. Trifirò, Structure sensitivity of the catalytic oxidation of n-butane to maleic anhydride. Chem. Commun. (8) (1985) 492-494. https://doi.org/10.1039/C39850000492

[44] K.H. Lii, L.F. Mao, Hydrothermal synthesis and structural characterization of a nickel (II) Vanadyl (IV) phosphate hydrate: $Ni_{0.5}VOPO_4 \cdot 1.5\ H_2O$. *J. Solid State Chem, 96 (1992)* 436-441. https://doi.org/10.1016/S0022-4596(05)80278-6

[45] R.C. Haushalter, V. Soghomonian, Q. Chen, J. Zubieta, Hydrothermal synthesis and crystal structure of $[Ni(H_2O)_4][VO(PO_4)]_2$, a nickel(II) vanadyl (IV) phosphate. *J. Solid State Chem, 105 (1993)* 512-519. https://doi.org/10.1006/jssc.1993.1243

[46] J. Lee, P. Srimuk, R. Zwingelstein, R.L. Zornitta, J. Choi, C. Kim, V. Presser, Sodium ion removal by hydrated vanadyl phosphate for electrochemical water desalination. *J. Mater. Chem. A, 7 (2019)* 4175-4184. https://doi.org/10.1039/C8TA10087J

[47] S. De, A. Dey and S. De, Characterization and electrical properties of vanadyl phosphate-polypyrrole nanocomposites. Journal of Physics D: Applied Physics, 39 (2006) 500. https://doi.org/10.1088/0022-3727/39/3/013

[48] L. Griesel, J. K. Bartley, R. P. K. Wells and G. J. Hutchings, Preparation of vanadium phosphate catalysts from $VOPO_4 \cdot 2H_2O$: effect of $VOPO_4 \cdot 2H_2O$ preparation on catalyst performance. J. Mol. Catal. A: Chem., 220 (2004) 113-119. https://doi.org/10.1016/j.molcata.2004.02.027

[49] N. Yamamoto, N. Hiyoshi, T. Okuhara, Thin-Layered Sheets of $VOHPO_4.\ 0.5H_2O$ Prepared from $VOPO_4.\ 2H_2O$ by Intercalation− Exfoliation− Reduction in Alcohol. *Chem. Mater, 14* (2002) 3882-3888. https://doi.org/10.1021/cm020292y

[50] W.S. Dong, J.K. Bartley, N.X. Song, G.J. Hutchings, Synthesis and characterization of vanadyl hydrogen phosphite hydrate. *Chem. Mater, 17* (2005) 2757-2764. https://doi.org/10.1021/cm0477568

[51] Z. Luo, E. Liu, T. Hu, Z. Li and T. Liu, Effect of synthetic methods on electrochemical performances of $VOPO_4 \cdot 2H_2O$ supercapacitor. Ionics, 21 (2015) 289-294. https://doi.org/10.1007/s11581-014-1317-7

[52] N.C.S. Selvam, R.T. Kumar, L.J. Kennedy, J.J. Vijaya, Comparative study of microwave and conventional methods for the preparation and optical properties of novel MgO-micro and nano-structures. *J. Alloys Compd*, *509* (2011) 9809-9815. https://doi.org/10.1016/j.

[53] S. Hidaoui, N. Hamdi, M. Akouibaa, R. Benali-Cherif, E. Vaclav, M. Dusek, M. Lachkar, B. El Bali, Synthesis, crystal structure and catalytic activity of the new hybrid phosphate $(C_4H_{12}N_2)[Co(H_2O)_6](HPO_4)_2$, J. Mol. Struct., 1265 (2022) 133296. https://doi.org/10.1016/j.molstruc.2022.133296

[54] H.O Hassani, M. Akouibaa, S. Rakass, M. Abboudi, B. El Bali, M. Lachkar, F. Al Wadaani, A simple and cost-effective new synthesis method of copper molybdate CuMoO4 nanoparticles and their catalytic performance, J. Sci. Adv. Mater. Devices 6 (2021) 501–507, https://doi.org/10.1016/j.jsamd.2021.06.003.

[55] P. Blaha, K. Schwarz, F. Tran, R. Laskowski, G. K. H. Madsen, and L. D. Marks, "WIEN2k: An APW+ lo program for calculating the properties of solids," J. Chem. Phys. 152 (2020). https://doi.org/10.1063/1.5143061.

[56] Z. Charifi, H. Baaziz, and A. H. Reshak, "Ab-initio investigation of structural, electronic and optical properties for three phases of ZnO compound," Phys. Status Solidi Basic Res., vol. 244 (2007) 3154–3167. https://doi.org/10.1002/pssb.200642471.

[57] A. Jain, G. Hautier, S.P. Ong, C.J. Moore, C.C. Fischer, K.A. Persson, G. Ceder, (2011). Formation enthalpies by mixing GGA and GGA+ U calculations. *Physical Review B*, *84*(4), 045115. https://doi.org/10.1103/PhysRevB.84.045115.

[58] X. H. Zheng and J. X. Zheng, "On the use of Monkhorst-Pack scheme to evaluate superconductivity and the issue of umklapp electron-phonon interactions," Phys. Chem. Chem. Phys. **25 (**2023) 13049-13060. https://doi.org/10.1039/d3cp01053h.

[59] A. Soussi, A. Ait hssi, L. Boulkaddat, A. Asbayou, N. Labchir, A. Elfanaoui, R. Markazi, K. Bouabid, A. Ihlal, A. Taleb, Structural, optical and electronic properties of La-doped ZnO thin films: Experimental study and DFT calculations, Physica B: Condensed Matter 643 (2022) 414181. https://doi.org/10.1016/j.physb.2022.414181.

[60] A. Soussi, A. Elfanaoui, A. Ait hssi, M. Taoufiq, A. Asbayou, L. Boulkaddat, N. Labchir, R. Markazi, A. Ihlal, K. Bouabid, Morphological, structural, electronic and optical properties of deposited 4d-Mo doped TiO2 thin films compared to first-principles calculations, Materials Today Communications 36 (2023) 106520. https://doi.org/10.1016/j.mtcomm.2023.106520.

[61] A. Ait hssi, A. Soussi, N. Labchir, M. Taoufiq, H. Najih, A. Elfanaoui, A. Ihlal, K. Bouabid, A DFT theoretical and experimental study of the effect of indium doping within

electrochemical deposited ZnO 217(2023) 112503.
https://doi.org/10.1016/j.vacuum.2023.112503.

Table 2: Fractional atomic coordinates and isotropic or equivalent isotropic displacement parameters (Å^2) for $[Mg(H_2O)_4][(VO)_2(PO_4)_2]$.

	x	*y*	*z*	U_{iso}*/U_{eq}
V	0.500000	0.500000	0.22293 (2)	0.00378 (8)
P	0.500000	0.000000	0.250000	0.00362 (9)
Mg	0.500000	0.500000	0.500000	0.00827 (16)
O1	0.48522 (9)	0.19730 (9)	0.18214 (4)	0.00631 (12)
O2	0.22272 (16)	0.32433 (18)	0.500000	0.01353 (18)
H1	0.151 (3)	0.328 (2)	0.4547 (11)	0.016*
O3	0.500000	0.500000	0.34217 (9)	0.0084 (2)

Table 3: Geometric parameters (Å, º) for $[Mg(H_2O)_4][(VO)_2(PO_4)_2]$.

V—O3	1.6002 (13)	P—O1	1.5357 (6)
V—O1	1.9716 (6)	Mg—O2	2.0514 (10)
V—O1^{i}	1.9716 (6)	Mg—O2^{vii}	2.0515 (10)
V—O1^{ii}	1.9716 (6)	Mg—O2^{viii}	2.0515 (10)
V—O1^{iii}	1.9716 (6)	Mg—O2^{iii}	2.0515 (10)
P—O1^{iv}	1.5357 (6)	Mg—O3	2.1180 (12)
P—O1^{v}	1.5357 (6)	Mg—O3^{vii}	2.1180 (12)
P—O1^{vi}	1.5357 (6)		

O3—V—O1	106.120 (18)	O2—Mg—O2^{viii}	90.0
O3—V—O1^{i}	106.119 (18)	O2^{vii}—Mg—O2^{viii}	90.0
O1—V—O1^{i}	85.580 (10)	O2—Mg—O2^{iii}	90.0
O3—V—O1^{ii}	106.119 (18)	O2^{vii}—Mg—O2^{iii}	90.0
O1—V—O1^{ii}	147.76 (4)	O2^{viii}—Mg—O2^{iii}	180.0
O1^{i}—V—O1^{ii}	85.579 (10)	O2—Mg—O3	90.0
O3—V—O1^{iii}	106.119 (18)	O2^{vii}—Mg—O3	90.0

O1—V—O1^{iii}	85.579 (10)	O2^{viii}—Mg—O3	90.0
O1^{i}—V—O1^{iii}	147.76 (4)	O2^{iii}—Mg—O3	90.0
O1^{ii}—V—O1^{iii}	85.579 (10)	O2—Mg—O3^{vii}	90.0
O1^{iv}—P—O1^{v}	110.59 (2)	O2^{vii}—Mg—O3^{vii}	90.0
O1^{iv}—P—O1^{vi}	107.26 (4)	O2^{viii}—Mg—O3^{vii}	90.0
O1^{v}—P—O1^{vi}	110.59 (2)	O2^{iii}—Mg—O3^{vii}	90.0
O1^{iv}—P—O1	110.59 (2)	O3—Mg—O3^{vii}	180.0
O1^{v}—P—O1	107.26 (4)	P—O1—V	127.08 (4)
O1^{vi}—P—O1	110.59 (2)	V—O3—Mg	180.0
O2—Mg—O2^{vii}	180.0		

Symmetry codes: (i) *y*, -*x*+1, *z*; (ii) -*x*+1, -*y*+1, *z*; (iii) -*y*+1, *x*, *z*; (iv) *y*+1/2, -*x*+1/2, -*z*+1/2; (v) -*x*+1, -*y*, *z*; (vi) -*y*+1/2, *x*-1/2, -*z*+1/2; (vii) -*x*+1, -*y*+1, -*z*+1; (viii) *y*, -*x*+1, -*z*+1.